THE UNIVERSITY OF CHICAGO

FLUORESCENCE INTERFERENCE CONTRAST MICROSCOPY, A NEW TOOL TO STUDY COLLECTIVE MOTOR DYNAMICS

A DISSERTATION SUBMITTED TO
THE FACULTY OF THE DIVISION OF THE BIOLOGICAL SCIENCES
AND THE PRITZKER SCHOOL OF MEDICINE
IN CANDIDACY FOR THE DEGREE OF
DOCTOR OF PHILOSOPHY

DEPARTMENT OF BIOCHEMISTRY AND MOLECULAR BIOLOGY

BY
AGATA K. KRENC

CHICAGO, ILLINOIS
AUGUST 2016

LIST OF CONTENTS

LIST OF FIGURES

LIST OF TABLES

LIST OF ABBREVIATIONS

ADP	adenosine diphosphate
AFM	atomic force microscopy
ATP	adenosine triphosphate
FIONA	fluorescence imaging with one nanometer accuracy
FLIC	fluorescence interference contrast
GFP	green fluorescent protein
HMM	heavy meromyosin
LMM	light meromyosin
NMIIB	non-muscle myosin IIB
P_i	inorganic phosphate
TIRF	total internal reflection fluorescence
TMR	tetramethyl rhodamine
YFP	yellow fluorescent protein

ACKNOWLEDGEMENTS

First, I would like to thank Dr. Ronald Rock for allowing me to perform research in his laboratory and providing guidance throughout my graduate school career. I thank my thesis committee members: Drs. Tobin Sosnick, Margaret Gardel and Sally Horne-Badovinac for their insight and guidance they provided over the last years. I would like to thank the members of the Rock lab and the Department of Biochemisty of Molecular Biology for sharing the experience and creating a great environment to grow. Special thanks to Alex French for his constant readiness to discuss my project and share his insight. I am very grateful for the advice, support and friendship I have received from Drs. Claire Atkinson and Brittney McClymmonds. I would like to thank the members of the Cytoskeleton Supergroup at University of Chicago for helpful discussion. Special thanks to Dr. Kim Weirich and Patrick McCall. The grad school would not be the same without my friends, who were the true support in the times of trouble and the best crowd to enjoy the good times. Special thanks to Jenny Lin for being my friend and roommate for most of my time in Chicago, Angika Basant for her perspective on life, Karolina Golab for being my strength and inspiration and Joe Brewer for being my favorite philosopher. Finally, I would like to thank my family, for the love and support they have given me for all my life.

CHAPTER 1: GENERAL INTRODUCTION

Actin cytoskeleton is a dynamic structure capable of supporting multiple cell functions. The processes of migration, cell and tissue shape maintenance, cell division and intracellular transport would not be possible without the coordinated action of actin, myosins and various actin binding proteins. The interplay between these elements gives rise to a complex and diverse cytoskeleton network. Myosins are important elements of this network playing fundamental roles in force generation, actin crosslinking and actin remodeling (Blanchoin et al., 2014; Murrell et al., 2015; Vicente-Manzanares et al., 2009).

1.1 MOLECULAR MOTORS – STRUCTURE AND FUNCTION

Myosins are molecular motors that hydrolyze ATP to power the movement along actin tracks (Howard, 2001). The myosin superfamily consists of at least 35 known myosin classes (Odronitz and Kollmar, 2007). Class II myosins (e.g. skeletal or smooth muscle myosins) are the best-studied members of the myosin superfamily. Because of their early discovery, they are frequently referred to as "conventional" myosins. The signature feature of conventional myosins is their functional unit, called the thick filament, composed of tens to hundreds of dimeric motors (Sellers, 2000).

The wealth of structural and biochemical work has been performed on class II myosins. Although currently we know many other myosin classes ("unconventional myosins"), the basic myosin blueprint and biochemical cycle described for class II members are shared within the myosin superfamily (de la Cruz and Ostap, 2004; Sellers, 2000;

Spudich and Sivaramakrishnan, 2010; Sweeney and Houdusse, 2010) (Figure 1). Myosins are composed of three main structural domains (Figure 1A). These are: the catalytic head (where the ATP hydrolysis takes place), the lever arm (a "rigid body" that propagates the small conformational changes occurring in the myosin head) and the tail domain (the most diverse domain that can allow for dimerization, oligomerization or cargo binding). As the myosin head progresses through its biochemical cycle (Figure 1B), conformational changes occur in the actin binding site (regulating the affinity to actin) and in the converter subdomain. Upon the release of an inorganic phosphate the converter subdomain transitions between the pre-powerstroke to the postpower stroke conformation. The lever arm propagates the swing of the converter and allows for a step along the actin filament (Figure 1 C). The lever arm structure varies for different myosin classes. It contains a variable number of conserved IQ motifs that are the binding sites for calmodulin or myosin light chains (Figure 1 C and Figure 2). The lever arm of myosin-6 contains a sequence (the unique insert) that switches a directionality of the conformational change propagation (Figure 1C)

Here, the structure and function of myosin 6, myosin 5 and Non-muscle myosin IIB (NMIIB), the three motors relevant for this thesis, are briefly described.

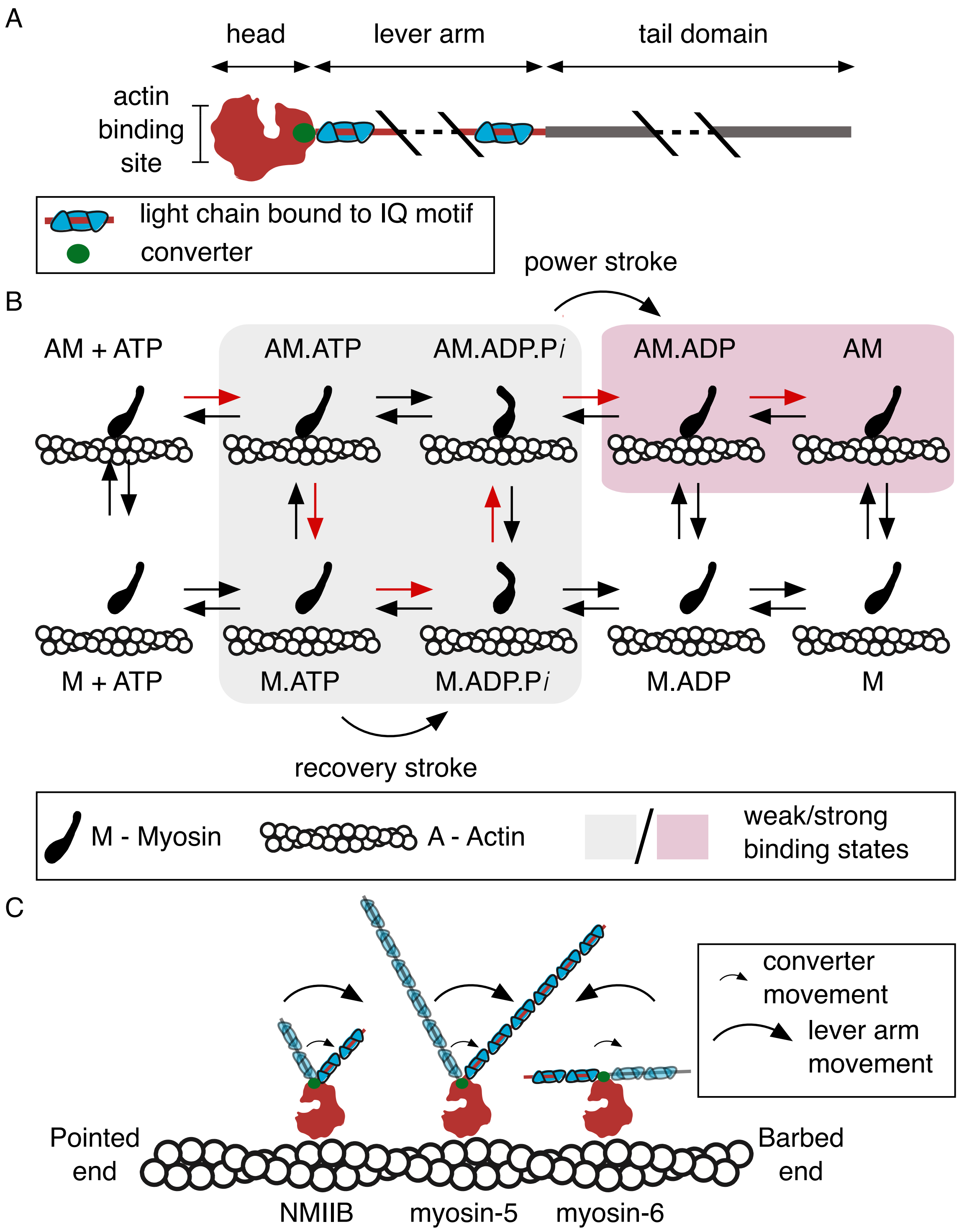

Figure 1. The structure and ATPase cycle of myosins. (A) General structure of a myosin a myosin. (B) The ATPase cycle of myosins. The hydrolysis of ATP and release of the reaction products is coupled to two mechanical steps: power stroke and recovery. stroke. The red arrows indicate the preferred pathway for the transitions. Gray shading indicates weakly bound states. Pink shading indicates strongly bound states.

Figure 1, continued. Figure based on (de la Cruz and Ostap, 2004). (C) Converter and lever arm swing in different myosin classes. Due to the unique structure myosin-6 lever arm, the power stroke has a switched directionality. Figure based on (Spudich and Sivaramakrishnan, 2010).

1.1.1 MYOSIN 6

Myosin-6 is the only known myosin motor walking towards the pointed end of actin (Wells et al., 1999). The unique structure of its lever arm (Figure 1C, Figure 2), with N-terminal part of the unique insert wrapping around the converter, allows for switched directionality (Spudich and Sivaramakrishnan, 2010; Wells et al., 1999). Although the isolated full-length myosin-6 is monomeric, it has been proposed that upon cargo binding it undergoes cargo-mediated dimerization (Park et al., 2006; Yu et al., 2009). *In vitro*, artificially dimerized myosin-6 is capable of walking hundreds of nanometers along the actin track (Okten et al., 2004; Zimmermann et al., 2015). Myosin-6 takes on average 30 nm steps, which suggest that part of its tail domain acts as a lever arm extension (Figure 2) (Rock et al., 2001; Spudich and Sivaramakrishnan, 2010; Yildiz et al., 2004).

In vivo, myosin-6 has been implicated in a wide range of functions. In *Drosophila melanogaster,* where it was discovered, myosin-6 was shown to play important role for a cleavage furrow ingression and mitotic spindle positioning during syncytial blastoderm mitosis (Kellerman and Miller, 1992; Mermall and Miller, 1995). A study of *D. melanogaster* spermatid individualization showed that myosin-6 is crucial for stabilization of branched actin network separating the developing sperm cells from the excluded organelles (Noguchi et al., 2006). The mouse model lacking the myosin-6 gene (Snell's waltzer mice) showed defects in the development of the sensory hair cells. In the mutant mice, the specialized cell protrusions called stereocilia show progressive disorganization of their actin filament bundles, which eventually fuse together. Myosin-6 has been suggested to function as an anchor, pinning the apical cell membrane between the individual stereocilia to the actin network (Self et al., 1999). Also, the experiments performed in fibroblastic cell line derived from Snell's waltzer mice show that myosin-6 plays a role in maintaining the morphology of the Golgi complex, possibly by anchoring its membrane to the actin cytoskeleton (Warner et al., 2003). Last but not least, myosin-6 has been shown to associate with clathrin-coated and uncoated vesicles and is an important factor mediating endocytosis (Aschenbrenner et al., 2004; Buss et al., 2001).

1.1.2 MYOSIN 5

Myosin-5 is possibly the best-studied unconventional myosin. The characteristic feature of myosin-5 is a long neck domain, composed of six IQ motifs that bind calmodulin or myosin light chains (Figure 2) (Cheney et al., 1993). The myosin-5 heavy chain forms a dimer through its coiled-coil tail domain (Cheney et al., 1993; Hammer and Sellers, 2012; Thirumurugan et al., 2006). It has been shown in *in vitro* experiments that dimeric myosin-5 can travel a distance up to few micrometers before detachment (Amit D Mehta et al., 1999; Zimmermann et al., 2015). The long neck domains allow the dimeric myosin to take ~36 nm steps, corresponding to pseudo-repeat of the actin filament (Amit D Mehta et al., 1999). Walking in a straight path, as opposed to spiraling along the long pitch of actin filament, is an example of an adaptation of myosin-5 for its intracellular function as a cargo transporter.

In animal cells, myosin-5 pulls the ER membrane into the dendritic spines of Purkinje neurons. The correct localization of ER in these cells is required for synaptic plasticity underlying motor learning in cerebellum (Wagner et al., 2011). Considering that many class V members (as well as class XI members that are plant counterparts) were shown to transport ER in different organisms, this might be an evolutionarily conserved function of myosin-5 (Hammer and Sellers, 2012). Myosin-5 is also responsible for the accumulation of melanosomes in dendrites and dendritic tips of melanocytes – the process underlying pigmentation in animals. During the accumulation, melanosomes are transported along the dendrite by bidirectional, long-range, microtubule-dependent transport and subsequently they are captured and distributed by myosin-5 in cell periphery (Wu et al., 1998). The role of myosin-5 is also very well documented in yeast where it was shown to transport secretory vesicles, late Golgi vesicles, vacuoles, peroxisomes and mRNA (Hammer and Sellers, 2012).

1.1.3 NON-MUSCLE MYOSIN II

Non-muscle myosin IIs (NMIIs) are class II myosin members, ubiquitously expressed in eukaryotic cells (Sellers, 2000). They form short thick filaments (comprised of ~ 30 myosin dimers, Figure 2) which crosslink actin filaments and organize the cytoskeleton in a network-like structure in the lamellum and the cell cortex (Blanchoin et al., 2014; Niederman and Pollard, 1975; Rochlin et al., 1995; Verkhovsky and Borisy, 1993). NMII thick filaments are also present in stress fibers and transverse arcs where they align with the long axis of the fiber and generate the contractile forces (Blanchoin et al., 2014; Murrell et al., 2015).

In mammals, there are three main isoforms of non-muscle myosins: NMIIA, NMIIB and NMIIC (Vicente-Manzanares et al., 2009). NMIIB and NMIIA are frequently expressed in the same cell types, where they have related but distinct functions. Interplay of both motors is crucial for cell migration. It has been shown that that NMIIA localizes to the front of the lamellum where it confers retrograde actin flow and protrusion retraction (Cai et al., 2006; Vicente-Manzanares et al., 2008, 2007), while NMIIB is present in perinuclear region and is responsible for front-back polarization and maintaining the direction of cell migration (Lo et al., 2004; Vicente-Manzanares et al., 2008). NMIIB plays role in cytoskeleton tension maintenance and is crucial for force generation during sustained state of smooth muscle contraction (Morano et al., 2000; Rhee et al., 2006). Non-muscle myosin II is also involved in cytokinesis, where it provides force for cleavage furrow ingression (Straight et al., 2003).

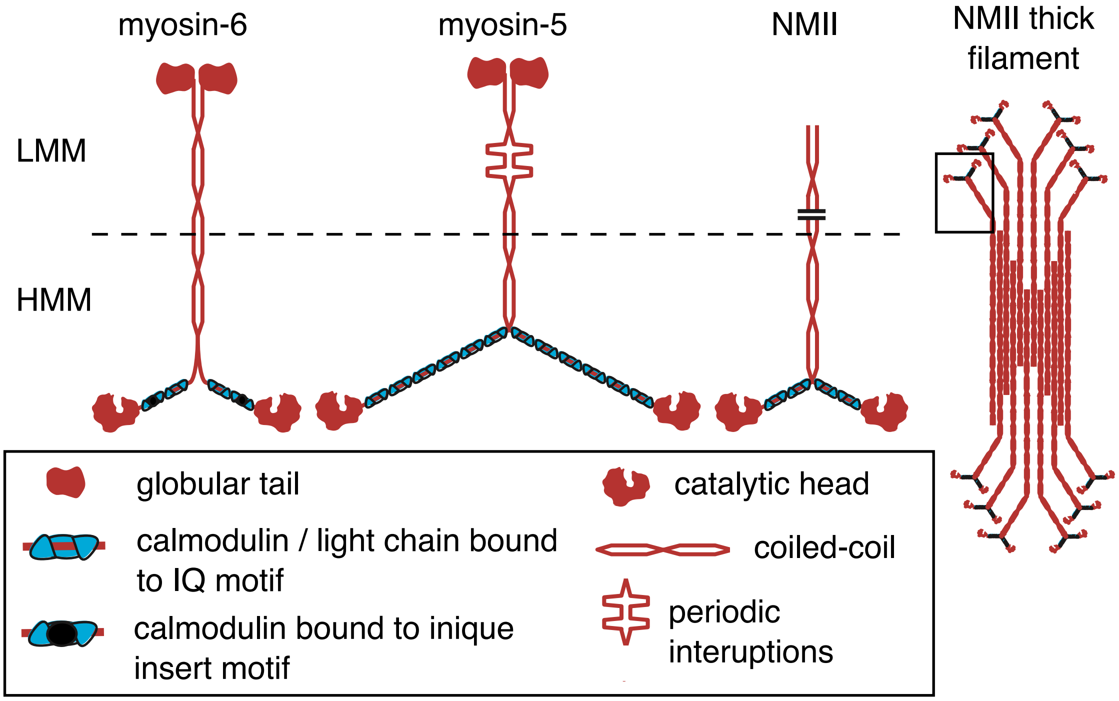

Figure 2. The structural differences between myosin-6, myosin-5 and NMIIB. Dimer is a functional unit of myosin-6 and myosin-5. NMIIs form thick filaments consisting of ~ 30 dimers. The myosins dimerize through their coiled-coil domain. HMM and LMM refer to the products of proteolitic digestion: heavy meromyosin and light meromyosin, respectively. HMM describes a dimeric motor, devoid of a large segment of its tail (including regulatory and cargo binding domains).

Until recently, NMIIs, like the rest of the class II myosins, were believed to be non-processive, meaning that they take just a single step along the actin filament before detaching (Sellers, 2000). However, optical tweezers studies of NMIIB and NMIIA have shown that both motors can take a few 5.5 nm steps along the actin track (Hundt et al., 2016; Norstrom et al., 2010).

1.2 METHODS TO STUDY MYOSIN FUNCTION

The cytoskeleton network can be studied on many different levels. The deletion strains in different organisms uncovered the functions of many myosins and actin binding proteins. The immunohistochemistry and transgene expression of GFP-fusion proteins revealed the tissue and subcellular localization of many molecular motors. Electron microscopy provided structural details of cytoskeleton organization, including the image of thick filaments of NMIIs (Niederman and Pollard, 1975). The studies of muscle fiber contraction gave us the initial understanding of myosin force generation capacity (Jewell and Wilkie, 1958). The bulk MgATPase and transient kinetic assays revealed the rate and equilibrium constants of individual steps in myosin biochemical cycle (Lymn and Taylor, 1971). Finally, functional *in vitro* motility assays, where purified actin and myosin were observed in a fluorescent microscope, facilitated our understanding of actin translocation and myosin mechanical cycle.

The new era for cytoskeleton has started in 1986 when Kron and Spudich published the first gliding filament assay (Kron and Spudich, 1986). In a gliding filament assay, myosins are immobilized to the glass cover slip and fluorescently labeled actin glides over the surface (Figure 3A). This simple assay allows for measurements of the gliding velocity driven by myosin ensemble. Because of highly controlled experimental conditions (purified proteins, easily adjustable buffer conditions) the assay allowed for reliable characterization of many molecular motors and the products of their enzymatic digestion (Toepfer and Sellers, 2014). However, gliding filament assay has limited application in the studies of individual events leading to a myosin walk.

Another milestone was achieved with the development of single molecule techniques. These techniques allowed for exploring the connection between ATP hydrolysis and the mechanical step of a myosin (Figure 1 B). The single molecule methods were fundamental in creating and reinforcing the current models of myosin function (e.g. swinging lever arm hypothesis, hand-over-hand stepping model, etc.). There are three most popular single molecule techniques used in the cytoskeleton field. These are: total internal reflection fluorescence microscopy (TIRF), optical tweezers and atomic force microscopy (AFM) (Veigel and Schmidt, 2011), each of which will be discussed in detail below.

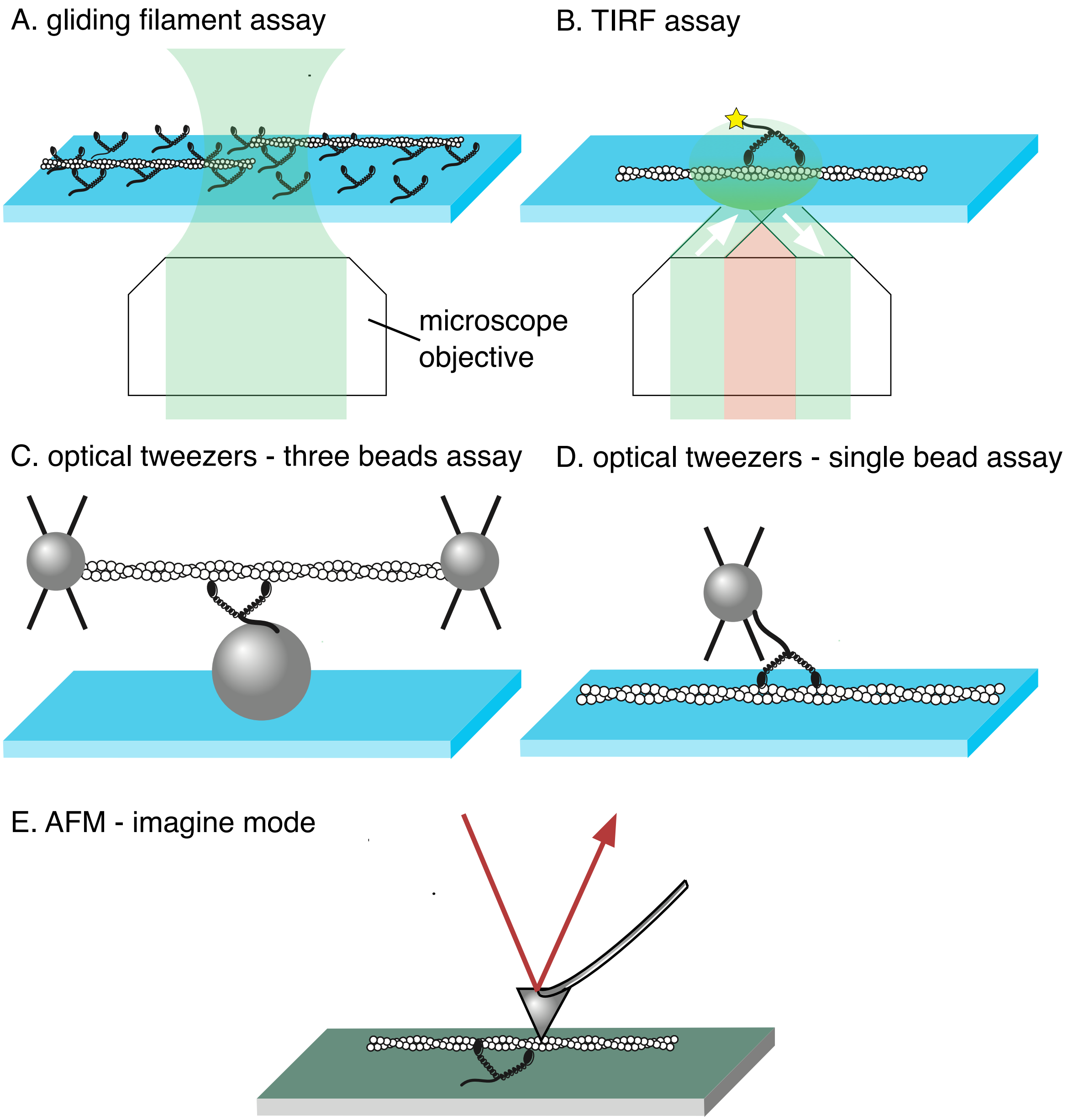

A. gliding filament assay

B. TIRF assay

C. optical tweezers - three beads assay

D. optical tweezers - single bead assay

E. AFM - imagine mode

Figure 3. Different methods to study myosins. (A) The gliding filament assay is usually performed in epi-illumination. (B) Total internal reflection fluorescence (TIRF) assay for low-background fluorescence imaging. C and D show two geometries popular when using optical tweezers. The crosses indicate the focus of the trapping laser. (C)Three beads assay. (D) Single bead assay. (E) AFM in the imaging mode. The sample is adsorbed on a substrate. The deflection of the AFM tip is detected by a reflection of a laser beam (red arrow).

1.2.1 TOTAL INTERNAL REFLECTION MICROSCOPY (TIRF)

TIRF microscopy relays on the phenomenon of total internal reflection of a laser beam at the boundary between a coverslip and a buffer (Figure 3B). When a laser light impinges upon the coverslip at the critical angle, it is reflected and it sets up an evanescent wave that penetrates 150 – 200 nm into the sample. The evanescent wave excites only the fluorophores in the proximity of the coverslip surface, dramatically improving signal to noise ratio. This allows for the observation of a single fluorophore. In a typical TIRF assay, actin filaments are immobilized to the surface of a coverslip and fluorescently labeled myosin motors are in solution. Individual myosin landing events and subsequent runs along the filament can be observed in TIRF microscopy (Toepfer and Sellers, 2014). Since TIRF microscopy was introduced to the cytoskeleton field around the turn of the XXI century (Sakamoto et al., 2000; Tokunaga et al., 1997) a number of discoveries were made that advanced our understanding of the myosin function.

In 2003, Yildiz et. al. fitted a diffraction limited image of a fluorophore (point-spread function, PDF) to a 2-dimentional Gaussian function, to obtain sub-pixel resolution. This technique, called FIONA (fluorescence imaging with one-nanometer accuracy), was used to discriminate between two models of myosin-5 stepping: the hand-over-hand model and the inchworm model. When only one lever arm in a dimer was labeled with a fluorophore, the step size distribution was consistent with the two heads alternating position - strongly supporting hand-over-hand model (Yildiz et al., 2003). The tight coupling between biochemical and mechanical cycle was demonstrated for myosin-5 using TIRF microscopy (with FIONA analysis) where the position of motor heads and the nucleotide state were monitored simultaneously (Sakamoto et al., 2008). The TIRF microscopy was used to report the step size of myosin-6 (Yildiz et al., 2004), the length of a processive run of myosin-10 along actin filaments and actin bundles (Nagy et al., 2008), the behavior of myosin-5 and myosin-6 at the filament-bundle intersection (go straight/turn/detach) (Ali et al., 2013) and many, many other aspects of myosin stepping behavior.

1.2.2 OPTICAL TWEEZERS

Optical tweezers are an experimental technique allowing for displacement and force measurements. A dielectric particle (e.g. plastic bead) placed in a focus of a trapping laser beam will experience a force (the gradient force) that will push the particle towards the laser focus, where the light intensity is the highest. This phenomenon can be exploited to manipulate the position of the particle by adjusting the position of the laser trap (Howard, 2001).

Since the first report on particle tapping by radiation pressure from a laser beam (Ashkin et al., 1986), the optical tweezers were widely used to study molecular motors. The reports showing the application of optical tweezers for the characterization of bacterial flagella (Block et al., 1989) and kinesin stepping model (Block et al., 1990) were released just few years after the initial, proof-of-principle report. The optical tweezers technique can be easily combined with fluorescence microscopy, making it very useful scientific tool. Over the last twenty years it allowed for many prominent discoveries in the myosin field.

There are several configurations in which an assay can be performed. In the three-bead assay (Figure 3C) myosin is immobilized to the larger (usually ~ 1.5 μm in diameter) surface bead. To ensure single molecule conditions the immobilization concentration is adjusted so that only 10-20% of the surface beads have myosin on them. Two other (smaller) beads are captured from the solution in the optical tweezers and actin filament is stretched between them to form a dumbbell (Figure 3C). When dumbbell is brought close to the surface bead with myosin on it, the motor starts pulling the actin, causing the displacement of trapped beads. This geometry was employed for early characterization of myosin-5 (A. D. Mehta et al., 1999). In these studies the displacement of trapped beads allowed for step size measurements and load-dependent dwell time measurements (time between the consecutive steps of myosin). The force (or load) can be measured in an optical tweezers, because within a certain distance from the laser focus (~ 200 nm), the trap will behave like a spring. The force experienced by the trapped bead can be calculated knowing its position relative to the trap center and the spring constant of the trap (Howard, 2001). The three-bead assay has an excellent temporal and spatial resolution. Therefore it can be used to investigate the behavior of marginally processive motors, like NMIIB (Norstrom et al., 2010) and non-processive motors, like skeletal muscle myosin II (Capitanio et al., 2012). In the later case, due to application of the ultrafast force-clamp (moving the position of the optical trap to the pre-set locations), the actin-myosin interactions as short as few tens of microseconds could be detected, revealing two pathways of premature detachment (before the power stroke) (Capitanio et al., 2012). Alternatively, a single-bead assay can be used to study processive myosins. In a single-bead assay, an actin track is immobilized to the surface and myosin-coated beads are optically trapped and brought into the proximity of the filament (Figure 3D). This approach has been frequently used to study myosin-5 (Clemen et al., 2005; Gebhardt et al., 2006).

1.2.3 ATOMIC FORCE MICROSCOPY (AFM)

Atomic force microscopy (AFM) allows for acquisition of high-resolution images without the need of sample staining. The technique can be used in imaging mode or force spectroscopy mode (Veigel and Schmidt, 2011).

In the tapping imaging mode (Figure 3E), the studied sample is mounted to the flat substrate surface (e.g. mica or planar lipid bilayer) and the cantilever is driven to oscillation up and down over the surface. As the cantilever tip taps over the scanned area it interacts with the sample. The deflection of the tip is detected by the laser beam reflection from the back of the AFM tip. High-speed AFM allows capturing single - nanometer resolution images at the video frame rate (within 100 ms or less) (Ando et al., 2013; Veigel and Schmidt, 2011).

Probably the most spectacular application of high-speed AFM in the myosin field is the study of myosin-5 processive walk along actin filament (Kodera et al., 2010) (Figure 4). The real time, high-resolution images of walking myosin-5 provided a direct evidence of hand-over-hand mechanism of myosin stepping. The level of structural details provided by these studies led to better understanding of molecular scale events underlying the motor function.

The single-molecule force spectroscopy mode was used to show that skeletal muscle myosin coiled-coil is an elastic protein, undergoing entirely reversible structural transition at forces 20-25 pN (Schwaiger et al., 2002).

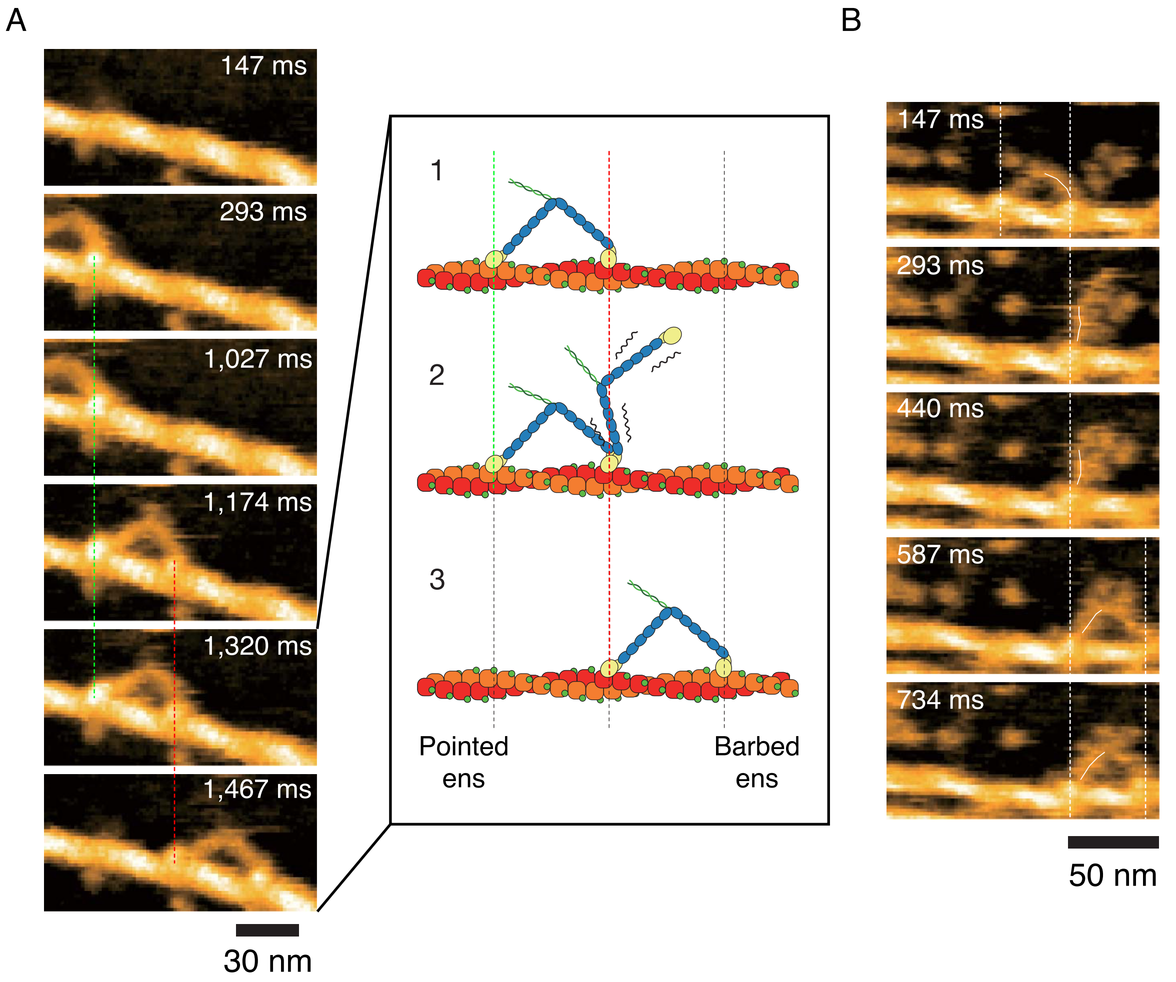

Figure 4. AFM imaging of Myosin-5 walk. (A) Myosin-5 alternates the head in the lead (hand-over-hand model). The green and red vertical lines connect actin heads bound to the same spot on actin, in the subsequent frames. The two last frames show the positions of the back (green line) and the front (red line) head before and after the power stroke of the leading head (corresponds to the cartoon 1 and 3, respectively). (B) Few frames from the movie showing an intermediate stage in myosin head transition (corresponding to cartoon 2 in A). A white line highlights the contour line of a swinging lever arm. Reproduced (and adapted) with permission from (Kodera et al., 2010).

1.3 SINGLE MOLECULE VERSUS ENSEMBLE BEHAVIORS

The single molecule studies have transformed the cytoskeleton field. Thanks to the advanced microscopy techniques (shortly described above) we could investigate the molecular mechanism of myosin function. However, inside a cell, molecular motors are believed to perform their tasks in small teams (Gross et al., 2007). Therefore to fully understand the myosin function *in vivo* we need to learn how the myosins cooperate with each other.

Many myosin-driven processes are shown or suggested to be performed by groups of motors. The functional form of NMIIs is an oligomer (thick filament) of ~30 myosin dimers (Niederman and Pollard, 1975). Also, intracellular transport is most likely carried out by multiple myosins. The vesicles obtained from ER extraction are coated with myosin-5. Depending on a size of the vesicle, the number of myosin-5s associated with the ER membrane is between 6 (for small ~100 nm vesicles) to 120 motors (for large ~1 µm vesicles) (Tabb et al., 1998). It has been estimated that there are on average 2 myosin-6 molecules associated with 100 nm clathrin-coated vesicles (Buss et al., 2001). The ability of different myosins to cooperate might be an important aspect of regulation of intracellular traffic.

The single molecule studies provide powerful predictors of motor ensemble dynamics. Berger and colleagues developed a theoretical description of the 2-motors behavior (Berger et al., 2012). The authors predict 4 different transport regimes based on the values of: elastic coupling between the motors, the stall force of a motor F_s (the force at which a motor cannot take a forward step), the detachment force of a motor F_d , the step size, velocity and unloaded detachment rate. Different combinations of these parameters result in: (I) a weak coupling (unaffected velocity and attachment lifetime to the molecular track), (II) strong coupling (reduced velocity and attachment lifetime), (III) reduced velocity regime (reduced velocity, unaffected attachment lifetime) and (IV) enhanced unbinding (unaffected velocity, reduced attachment lifetime). According to the theoretical calculations, kinesin-1 should be able to access the regime I, II and IV, while myosin-5 and myosin-6 should only be able to access the regimes I and III. Also, the comparison between myosin-5 and myosin-6 leads to the conclusion that myosin-6 remains in regime I over slightly broader range of elastic coupling (Berger et al., 2012).

The theory presented by Berger et. al. is consistent with the studies of two kinesin-1 motors linked by DNA scaffold (Rogers et al., 2009). The 2-kinesin ensemble moves with the velocity no different from the velocity of a single motor. Although the runlength of a 2-motor complex is longer than the runlength of a single kinesin-1, it is shorter than expected for two linked but non-interacting motors (negative interference of motors). Increased detachment of a second motor $k_{2\rightarrow1}$ is observed, leading to a single-kinesin state dominating over a two-kinesin state (Rogers et al., 2009). This study is a striking example of kinesin-1 falling into enhanced unbinding cooperation regime (regime IV). Similar studies on the dynamics of two linked myosin-5s, in the geometry presented in Figure 5A, showed reduced velocity of the complex (Lu et al., 2012) – the result consistent with regime III. However, the detachment rate of the second myosin $k_{2\rightarrow1}$ was slightly enhanced (measured $k_{2\rightarrow1}$ = 0.97 s^{-1} versus expected $k_{2\rightarrow1}$ = 0.75 s^{-1} if $k_{2\rightarrow1}= 2\ k_{1\rightarrow0}$), leading to attenuated runlength (comparing to model assuming no interaction between the motors) (Lu et al., 2012).

Although the knowledge of single molecule properties of a molecular motor is useful in interpreting the ensemble behavior *in vitro*, there are more factors that need to be considered. The effect of lipid composition of a vesicular cargo, vesicle diameter and motor density was studied for myosin-5-driven transport *in vitro* (Nelson et al., 2014), in the geometry presented in Figure 5B. Interestingly, these studies revealed the presence of fast population of vesicles (faster than a single myosin) for fluid-like vesicles. The enhanced velocity was attributed to preferential motor detachment at the trailing edge of a vesicle and vesicle snapping to the new center-of-mass position (Nelson et al., 2014).

Another aspect of the intracellular transport that has not been addressed so far is the behavior of the actin track. To our knowledge, all the currently existing models of myosin cooperation treat actin filament as a rigid rod. At the cellular scale this might not always be the correct treatment, as the actin filament is a semiflexible polymer with the persistence length comparable to the cell dimensions (L_p = 9 μm (H Isambert et al., 1995)).

Entirely different ensemble behaviors are expected for non-processive myosins. It has been shown that for skeletal muscle myosin II the siding velocity (measured in the gliding filament assay) increases with the surface density of motor (Uyeda et al., 1990). Walcott et al. explored the nature of this phenomenon using the theoretical model based on single molecule measurements and computer simulations. Their results suggest that the internal forces between myosins pulling the same filament decreases the attachment lifetime and increase the attachment distance (the distance each head travels while bound to actin) (Walcott et al., 2012).

One challenge in the ensemble measurements is that the location of the force-generating myosin motors is not always known. For example, in the typical gliding filament assay, only the actin filament motion is monitored over invisible, unlabeled myosins. Next, I will introduce a technique that can overcome this experimental obstacle.

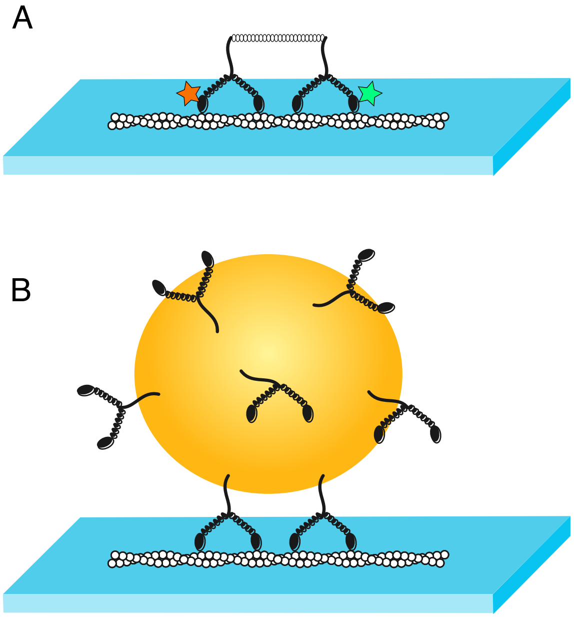

Figure 5. Experimental design used for studies of myosin cooperation. (A) The design used in (Lu et al., 2012). Two myosins, each labeled at one monomer, were linked by DNA string and observed in TIRF assay. (D) The design used in (Nelson et al., 2014). YFP-Myosin-5 was linked to vesicles of known lipid compositions and imaged in TIRF microscope. The average number of myosins per vesicle was quantified.

1.4 FLUORESCENCE INTERFERENCE CONTRAST MICROSCOPY (FLIC) – A VERSATILE METHOD TO STUDY THE CYTOSKELETON

Fluorescence interference contrast microscopy (FLIC) is a powerful technique, introduced to the cytoskeleton field in the last decade. It allows for the measurements of absolute distance from the reflective surface. The measurements can be performed with 1 nm precision, and they can be performed using simple fluorescent microscope. Here, the theory behind it and selected applications are reviewed.

1.4.1 THE PRINCIPLE OF FLIC AND ITS APPLICATION TO THE BIOLOGICAL SYSTEM

In 1996, Armin Lambacher and Peter Fromherz described the optical theory underlying the fluorescence intensity change with a distance between a fluorophore and a reflective silicon surface (Lambacher and Fromherz, 1996). In the relationship they derived, the observed fluorescence intensity I_{FLIC} is proportional to the probability of excitation and emission

$$I_{FLIC} \propto P_{ex} P_{em}$$

where both probabilities depend on the distance of the fluorophore to the reflective surface.

In the simplest scenario (Figure 6A), a fluorophore molecule is embedded in transparent silicon oxide (refreactive index n_1), at a distance d from the reflective surface of a silicon chip (refreactive index n_0). The unit vector e_{ex} describes the orientation of the transition dipole of excitation. When the fluorophore is illuminated by light of a wavelength λ_{ex}, the probability of excitation per unit time P_{ex} is proportional to the square projection of the normalized local electrical field F_{in} of the incident wave on the direction of the transition dipole $|F_{in} e_{ex}|^2$. The local electric field F_{in} is affected by the interference between the wave arriving to the fluorophore directly from the source and the wave reflected of the silicon surface. The phase difference Φ_{in} between these two waves is given by

$$\phi_{in} = \frac{4\pi n_1 d \cos\theta^{in}}{\lambda_{ex}}$$

where θ^{in} is a angle of incidence (Figure 6A). From the equation above it can be read that the phase difference is proportional to the distance from the reflective surface divided by the wavelength d/λ_{ex}. The local electric field value, F_{in}, is corrected by the change in amplitude between the incident and reflected ray taking place at the interface between the silicon/silicon oxide (given by Fresnel coefficients). The final expression for the probability of excitation P_{ex} depends on the average of the $|F_{in}e_{ex}|^2$, when the parameters like coherence of the excitation light, incident angle of excitation light (θ^{in}), polarization angle of the excitation light (γ_{in}) and the angle of the transition dipole of the fluorophore (θ_{ex}) are varied. The average $\langle|F_{in}e_{ex}|^2\rangle$ is integrated over the spread in excitation wavelength giving the final proportionality

$$P_{ex} \propto \int d\lambda_{ex}\, I(\lambda_{ex})\, \epsilon(\lambda_{ex}) \langle|F_{in}e_{ex}|^2\rangle$$

where $I(\lambda_{ex})$ is the intensity and $\epsilon(\lambda_{ex})$ is the extinction coefficient of the fluorophore at the wavelength λ_{ex}. The emission light undergoes the same processes. The probability of emission is given by

$$P_{em} \propto \int d\lambda_{em}\, \Phi_{det}(\lambda_{em})\, f(\lambda_{em}) \langle|F_{out}e_{em}|^2\rangle$$

where $\Phi_{det}(\lambda_{em})$ is the quantum yield of the detector and $f(\lambda_{em})$ is the fluorescence spectrum.

The theoretical model described by Lambacher and Fromherz was in excellent agreement with the experimental data, (Figure 6B) and FLIC was shown to detect changes in a surface profile on the order of magnitude of one nanometer (Lambacher and Fromherz, 1996).

Following this pioneering work, several reports were published, describing the application of FLIC for structural characterization of the neuronal cell adhesions (Braun and Fromherz, 1998), different preparations of supported lipid bilayers (Ajo-Franklin et al., 2005; Kiessling and Tamm, 2003) and the geometry of the t-SNARE/v-SNARE protein complex (Kiessling and Tamm, 2003).

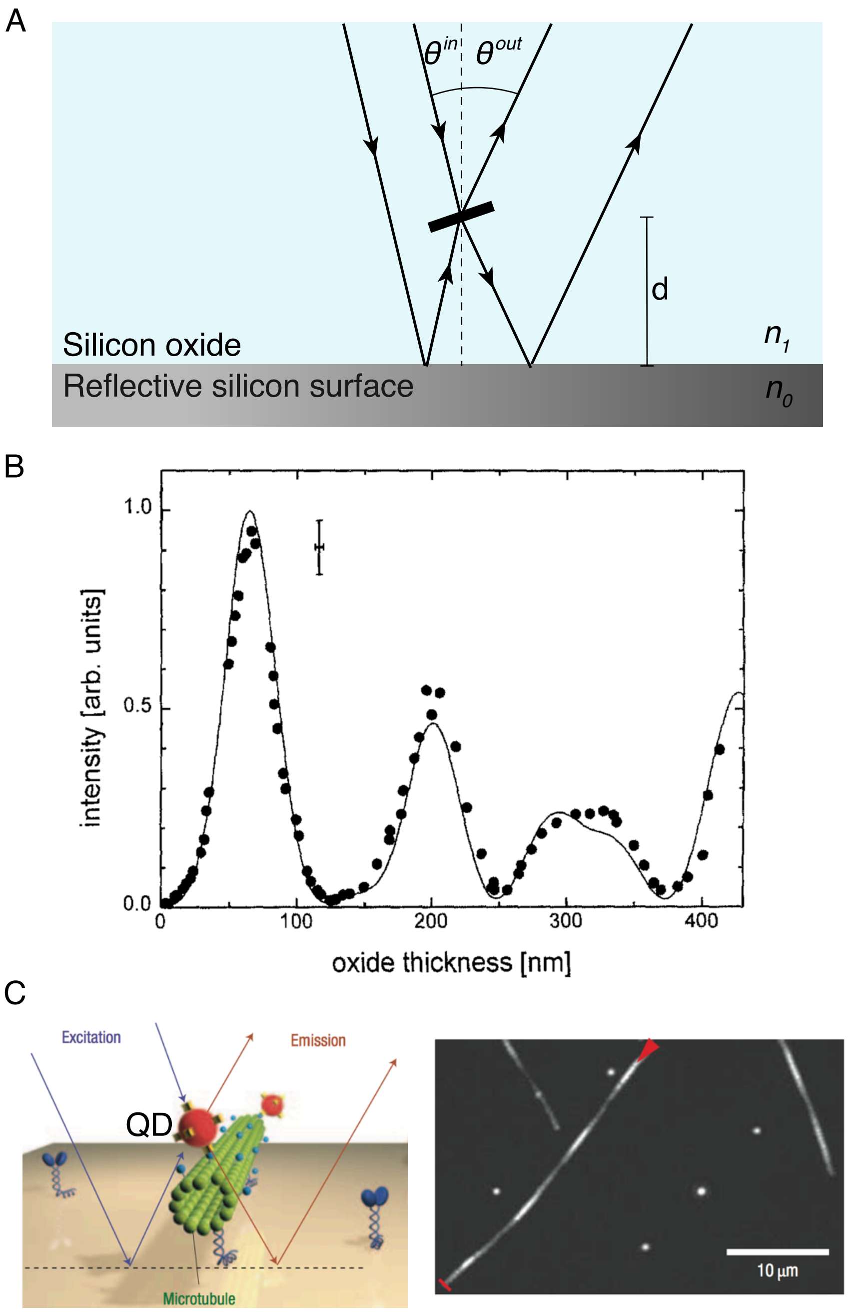

Figure 6. The principle of FLIC and its application. (A) The simple optical model. The incoming excitation ray can hit the fluorophophore embedded in silicon oxide layer coming directly from the source or after being reflected at the silicon surface. The emission (outward going) rays undergo the similar process. The figure adapted from (Lambacher and Fromherz, 1996) (B) The experimental (dots) and theoretical (line) values of fluorescence intensity of a cyanide dye as a function of distance to the reflective surface (d, oxide thickness) obtained by Lambacher & Fromherz (Lambacher and Fromherz, 1996). Reproduced with permission. (C) Application of FLIC for the

Figure 6, continued. studies of the torque imposed to microtubules by kinesin-1. The experimental design (left) and maximum intensity projection of a movie showing gliding microtubule (right). The rotation of a QD shows as a trace of periodically fluctuating fluorescence intensity. Reproduced with permission from (Nitzsche et al., 2008).

1.4.2 FLIC IN STUDIES OF MOTOR PROTEINS

The application of FLIC is not limited to measurements of the distances at the plasma membrane. The technique has been proven useful for studying molecular transport. Kerssemakers and coworkers immobilized kinesin-1 to the reflective surface and measured the height at which the motors hold fluorescently labeled microtubules – the molecular track for kinesins (Kerssemakers et al., 2006). This experimental set-up is a modern adaptation of gliding filament assay and extends the application of FLIC beyond pure distance measurements. The kinesin-1 driven transport was further explored by resolving the pitch of rotation of a microtubule sparsely labeled with quantum dots (Figure 6C). As the kinesin-1 follows a single, left-hand twisted protofilament, it repeatedly brings the individual quantum dots closer and further away from the surface as the microtubule rotates. It is visible in the assay as a path of bright and dim fluorescence (Figure 6C *right panel*) (Nitzsche et al., 2008). FLIC microscopy was also used to determine the adsorption geometries of different myosin preparations (HMM versus S1 constructs, S1 is a monomeric myosin consisting of the head and lever arm domains) on differently prepared surfaces (Persson et al., 2010). Importantly, theses recent applications of FLIC employ more empirical methods to relate the distance from the reflective surface to the fluorophore, creating a calibration curve.

1.5 THE PURPOSE OF THIS THESIS

The purpose of this thesis is to present novel application of FLIC microscopy. The FLIC assay described in chapter 2 and 3 is a modification of gliding filament assay. However, due to the interference of light, the locations of individual myosins are visible in the assay plane (with no need for myosin staining). This method allows for attachment lifetime measurements for the individual motors and better description of actin shape change during actin-myosin interaction. The FLIC assay allows for simultaneous measurements of a single myosin behavior and ensemble dynamics. It bridges the gap between the single molecule techniques and ensemble measurements making it well suited for the study of cooperation between the myosins. Moreover, in the FLIC assay the myosins are immobilized to the stiff substrate and they are mechanically coupled through the actin filament. This set-up is different than in the majority of studies of collective dynamics of processive motors. Unlike in the TIRF assay, where actin is tethered to the surface, in the FLIC assay, the myosin binding and translocation can alter the shape of the filament. My results reveal the robust buckling of actin at intermediate myosin immobilization concentrations. Such buckling of the actin cytoskeleton was proposed to be important for network contractility (Murrell et al., 2015). The implications of our findings for the regulation of the intracellular transport are discussed in chapter 4.

CHAPTER 2: THE COLLECTIVE MYOSIN DYNAMICS OF MYOSIN 6

2.1 INTRODUCTION

Myosins are molecular motors that hydrolyze ATP to power their movement along actin tracks [Howards 2001]. Multiple copies of class V (myosin-5) and class VI (myosin-6) myosins are associated with molecular cargos, suggesting that teams of processive motors govern intracellular transport (Buss et al., 2001; Gross et al., 2007; Tabb et al., 1998). Over the last fifteen years, development of single molecule techniques enabled the detailed studies of biophysical properties of a single motor (Veigel and Schmidt, 2011). However, a group of processive myosins can have very different properties from the individual myosins. The connection between the properties of a single myosin and a myosin assembly can be complex. How myosins behave when they are part of multi-motor assembly is an important question in the motor dynamics and cellular biology fields.

In vitro, an ensemble of motors typically demonstrates enhanced run-length and slower movement relative to a single motor (Berger et al., 2012; Hariadi et al., 2014; Lu et al., 2012). The critical role of collective motor behavior for the regulation of intracellular trafficking has been depicted by Efremov et. al (Efremov et al., 2014). They showed that myosin 5–driven transport, but not kinesin-1-driven transport, was sensitive to motor density. The addition of myosins increased the velocity of a cargo, although the velocity was still below that of a single myosin. These studies highlight the importance of effective load-sharing for the intracellular transport (Efremov et al., 2014).

Myosin-6 is the only known myosin that walks towards the pointed end of actin (Wells et al., 1999). It was originally discovered in *Drosophila melanogaster* and has been shown to be important in early *Drosophila* development (Kellerman and Miller, 1992; Mermall and Miller, 1995). Myosin-6 works in a wide range of cellular roles including active transport and regulation of endocytosis (Buss et al., 2001). It also serves a structural or anchoring role, for example in maintaining separated stereocilia (Self et al., 1999) or the maintenance of the correct morphology of the Golgi (Warner et al., 2003). The unique load-sensitivity of myosin-6 suggests a possible mechanism for its anchoring role at sub-saturating ATP conditions or in the presence of ADP (Altman et al., 2004). However, the load-sensitivity alone does not explain how myosin-6 could act as a vesicle transporter and anchor in the same cell, unless for each of these functions it experiences dramatically different load.

Here, I propose another mechanism of regulation of myosin-6 function, relying on its ability to effectively share the load between myosins carrying cargo along the same actin track. For a small cargo (e.g. endocytic vesicle) myosins are spaced close to each other, however for a large cargo (e.g., the Golgi apparatus) the myosins can be located further apart. Since actin is a semiflexible polymer capable of bending in a solution over a physiologically relevant range of lengths (H Isambert et al., 1995), the segment of actin can transduce a different amount of force for short and long separations. This could differentially regulate the activity of myosins, and they could be mechanically coupled or uncoupled from each other depending on the length of actin between them.

To address the question of myosin-6 collective behaviors as a function of the separation between the motors, I performed a series of experiments using fluorescence interference contrast microscopy (FLIC) (Kiessling and Tamm, 2003; Lambacher and Fromherz, 1996). FLIC measures the height of a fluorescently labeled actin filament above the surface in a gliding filament assay geometry. This allows for the detection of small changes in a filament contour line. The myosin attachments that tether actin to the surface are clearly visible in the assay. Therefore, using FLIC I can simultaneously observe the states of individual motors and the net product of their cooperation in a gliding filament assay. The data show that asynchronous myosin stepping leads to extensive actin buckling at intermediate myosin densities. However, as the density increases, the myosins coordinate their steps leading to short-lived buckles and decreased overall buckling.

2.2 THE FLIC GLIDING FILAMENT ASSAY DESIGN

In the FLIC assay, I immobilized myosin on a silicon wafer, and then monitored the transport of fluorescently labeled actin filaments in a gliding filament assay. I stabilized the actin filaments with a fluorescent phalloidin at saturation, achieving uniform filament labeling. The schematic representation of the experimental set-up is depicted in Figure 7A. The principle of FLIC is the interference of light emitted by fluorophores near a reflective surface. The interference causes the observed fluorescence intensity to change as a function of a distance between the fluorophore and the reflective surface. To demonstrate that in FLIC the fluorescence intensity of a uniformly labeled actin is a reporter of its height above the reflective surface, I prepared several silicon wafers that differ in thickness of a transparent silicon oxide layer (see Materials and Methods). Static actin filaments, tethered to the surface as in Figure 7A, vary in fluorescence intensity with the thickness of the silicon oxide layer. These filament intensity data were used to create a calibration curve (Figure 7B), used later in this chapter to determine the height of myosin-induced deformations. The peak of fluorescence observed in the FLIC calibration experiment corresponds to the height of ~82 nm above the surface, while the smaller heights result in dimmer fluorescence. This range and variation is consistent with previous reports (Kerssemakers et al., 2006; Nitzsche et al., 2008; Persson et al., 2010).

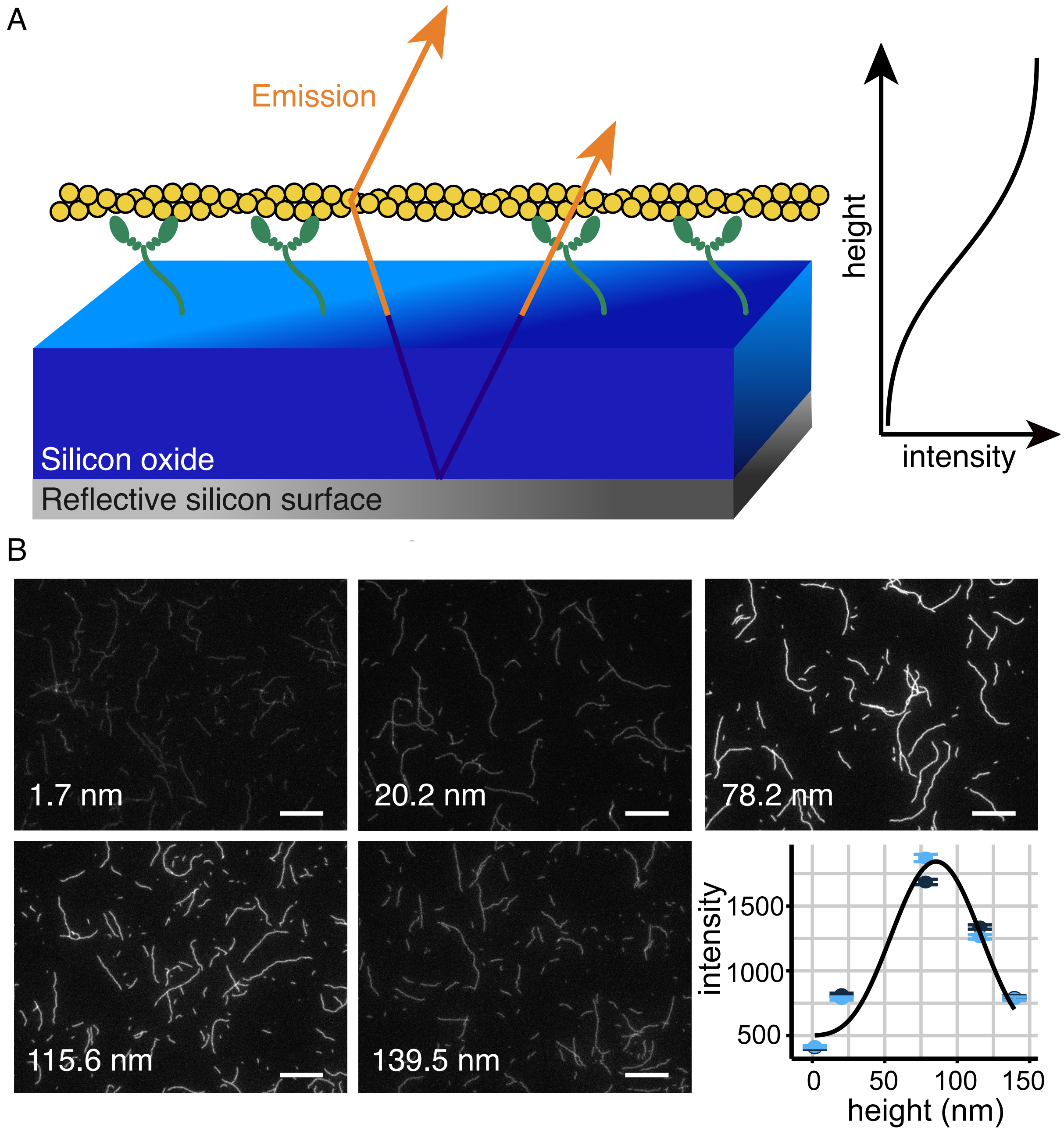

Figure 7. The FLIC assay measures distances between the fluorescently labeled actin and the Si/SiO_2 surface. (A) The FLIC assay geometry. Myosins (green) are immobilized on the surface of a silicon wafer and uniformly stained actin (yellow) adheres to the myosins. (B) FLIC calibration. Part of a single field of view from the

Figure 7, continued. microscope for each thickness of silicon oxide layer. We used the same preparation of actin for all oxide layer thicknesses shown. We applied myosin at 42 nM. Scale bar, 10 *μ*m. The lower right panel shows the calibration curve, relating the fluorescence intensity to the height in nm. Black and blue dots represent two sets of measurements performed on the same day. Error bars show standard error of the mean in each measurement.

In the following sections of this chapter (also in chapter 3) the thickness of the silicon oxide layer is constant within an experiment and the reported heights refer to the distance between the fluorescently labeled filament and the surface to which the myosins are immobilized (Figure 8A).

2.3 THE ASSIGNMENT OF MYOSIN POSITION IN THE FLIC ASSAY

In the FLIC gliding filament assay, the addition of ATP allows the myosin to perform mechanical work. This work can result in nanoscale actin deformations such as bending the actin filament between two myosin attachment points (Figure 8 A). These small changes in local actin height are detectable in the FLIC assay. The flexibility of actin filament provides a unique ability to identify the locations of myosin in the assay plane. In FLIC assay, surface-tethered myosins bind actin and bring it close to the reflective surface (Figure 8 *B-D)*. We can detect the location of a myosin from a short, dim segment of actin directly above the myosin. Figure 8B provides a striking example of myosin position assignment. In this sequence of images, a filament is pivoting about an attachment point: a damaged myosin-6 (red arrow). In frames 48.5 s – 61 s the filament is caught by a second, active myosin (green arrow). The active motor pulls actin into tension (straightened actin at the frame 61 s). Note that, for the rest of this manuscript, the generally rare damaged motors are excluded from the analysis.

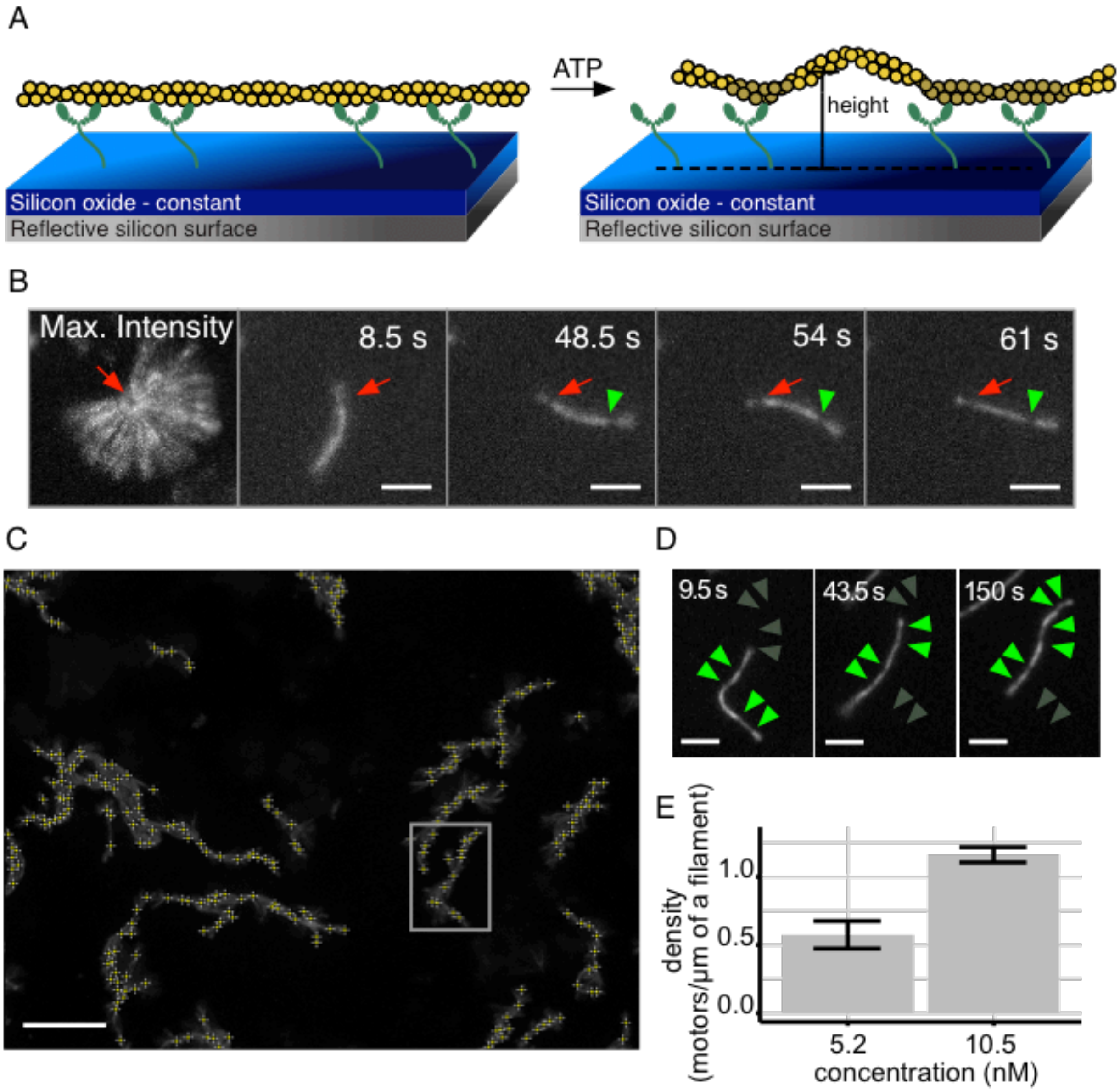

Figure 8. Myosin binding brings actin closer to the surface and reveals the myosin location. (A) The addition of ATP allows for actin gliding. The height/intensity changes reported from now on are the consequences of actin deformation and not changes in silicon oxide thickness. (B) The dim point shows the location of myosin. The panel shows a maximum intensity projection and frames from a movie showing a single actin filament attached to the surface by a single damaged myosin (red arrow) and, in some frames (48.5 s, 54 s, 61 s), by an active motor (green arrowhead). Scale bar, 3 *µ*m. (C) FLIC robustly detects the locations of myosins in a gliding filament assay. The image shows maximum intensity projection of a single field of view of a FLIC assay. The myosins can be identified in the regions where actin was gliding. The crosses show the assigned myosin locations. The rectangle identifies the region enlarged in C. Scale bar, 10 *µ*m. (D) Example of a filament revealing the positions of 8 myosin-6s. Scale bar,

Figure 8, continued. 3 μm. (E) The number of detected myosins is proportional to myosin concentration. The bar graph shows the surface densities of myosins derived from myosin counting and expressed as a number of myosins per 1 μm of a filament. Error bars show standard error of the mean.

A FLIC assay provides a robust and reliable detection method to identify and count myosins tethered to the surface, at low to intermediate myosin immobilization concentration (Figure 8C-E). Myosins were detected in all the regions where actin was gliding in the assay (Figure 8C). When the myosin was immobilized to the surface at half the initial protein concentration (5.2 nM versus 10.5 nM), we detected two times fewer myosins in our assay (Figure 8E). However, the relationship between myosin concentration and number of detected myosins is more complicated at higher myosin concentrations. Because of the resolution limit, the probability of undercounting the myosins increases.

2.4 MYOSIN-POWERED ACTIN DEFORMATION

Apart from the myosin location assignment, I can identify the segments of actin under tension and compression (Figure 9). Buckled segments of actin extend higher above the surface and they appear brighter in the FLIC assay (Figure 9*A*, segments between the yellow arrows). Occasionally, large buckles, extending beyond the first maximum of the calibration curve and out of focus can be observed, as in Figure 9*A* frame 71.5 s. In these large buckles, a characteristic pattern of bright edges and dim centers is visible, and the buckle appears flexible in the movie. In contrast, the segments of actin pulled into tension are brought closer to the surface and they appear dim and straight (Figure. 9*A,* segments between the red arrows). We argue that this dynamic pattern of actin deformation is an outcome of asynchronous myosin stepping leading to actin tension and compression. If the filament in Figure 9*B* travels toward the right (blue arrow) and myosin B stochastically takes more steps than both myosin A and myosin C, then the segment of actin ahead of myosin B will be under compression and will eventually buckle. The segment of actin behind myosin B will be under tension. Therefore the pattern of buckled and taut segments of actin informs us about the relative, momentary speeds of motors.

To measure the size of the buckles and to confirm their myosin-activity dependence, I scaled the fluorescence intensity of the filaments using the calibration curve shown in Figure 7B, in the presence and absence of ATP (Figure 9 C-F). The myosin attachments are visible in the kymographs as vertical lines corresponding to the heights oscillating around 0 -10 nm in Figure 9C and Figure 9E. This is consistent with the value obtained for fit parameter h = 10.44 nm, that describes the "myosin length" (see Materials and Methods), in the FLIC calibration. In the presence of ATP and at the 27.9 nM myosin immobilization concentration, the buckles reach as high as ~60 nm above the surface (Figure 9C) which is below the detection limit (82 nm, Figure 7B *lower right panel*). The pattern of buckled segments of actin and segments of actin pulled toward the surface is dynamic in Figure 9C. For comparison, when the filaments from the same slide were imaged without ATP, they were pulled close to the surface over almost the entire length of the filament, without dynamic changes in filament height (Figure 9D). These results show that myosin-6 stepping causes actin buckling. Our *in vitro* assay detects these actin deformations that are mostly undetectable in standard gliding filament assays.

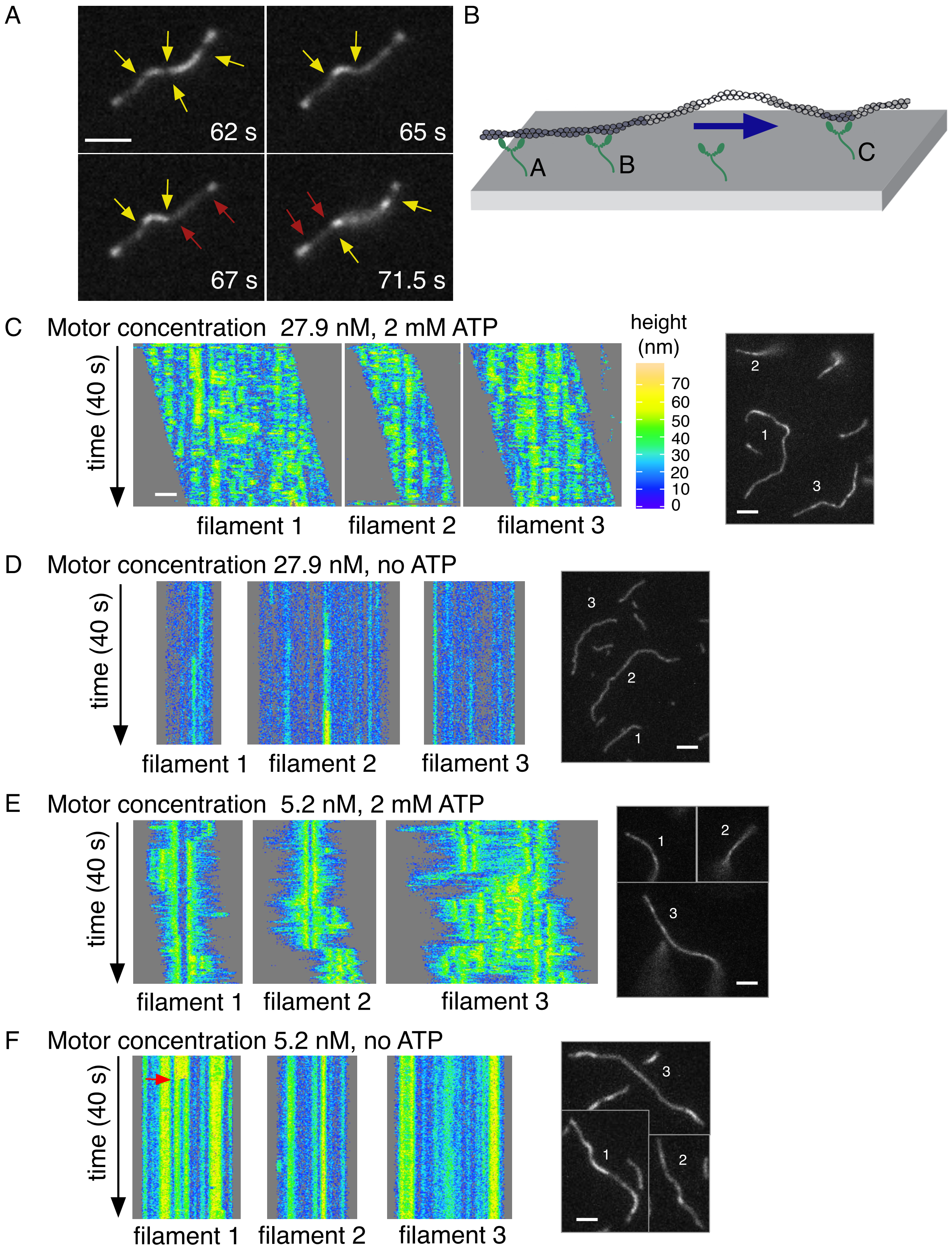

Figure 9. Asynchronous myosin stepping causes actin deformation. (A) FLIC reveals the state of actin between two bound motors. Frames showing the progression

Figure 9, continued. of a single actin filament pulled by myosin-6. Yellow arrows mark ends of actin segments buckled away from the surface between two engaged myosin-6 s. Red arrows mark ends of a segment of actin pulled into tension between two motors, and therefore pulled closer to the surface. The buckle in the last frame is large and is no longer in focus. Scale bar, 3 μm. (B) The model of dynamic actin deformation. The blue arrow shows the direction of actin motion. When myosin 2 takes more steps than myosin 3, excess actin accumulates between the two myosins, eventually forming a buckle. When myosin 2 takes more steps than myosins 1, the intervening segment is under tension. (C-F) The magnitude of myosin-induced actin deformation. Examples of actin filaments interacting with high (C and D) and low (E and F) densities of myosin-6, in the presence (C and E) and absence (D and F) of ATP. Colors in (C) indicate the height above the surface. Notice that in (C) the filaments are moving, indicated by the diagonal band in the kymographs. Myosin attachments are visible as vertical lines corresponding to the 0-10 nm heights. The pattern of buckled segments of actin and segments of actin pulled to the surface constantly changes with ATP, and is relatively static without ATP. At low myosin concentration in (E), single myosin attachment sites are clearly visible but the ends of actin project away from the surface and out of focus. Without ATP in (F), the filaments show many static buckles, which I interpret as a consequence of sequential binding to the myosins at low surface density. Notice the myosin binding event in filament 1 (red arrow). Scale bar 3 μm.

Interestingly, the filaments propelled by myosin at 5.2 nM immobilization concentration display a very different pattern of deformations (Figure 9E). The myosin attachment sites are very clear, however, they are so sparse that the edges of actin project away from the surface and are out of focus. The buckles are rare and they are long enough to exert a negligible force on the constraining myosins (see below). On the other hand, when only few motors are present at the surface in the absence of ATP, the filaments can be captured from the solution with buckles (Figure 9F). These buckles are static, with the exception of rare “new” binding events (Figure 9F, red arrow in filament 1).

Notice that the buckles have not been previously identified in a study of skeletal muscle myosin extension above the surface (Persson et al., 2010). We believe that the difference in myosin surface density (see later in a text) and /or the use of nonprocessive myosin-2 vs. processive myosin-6 could account for the difference between these two reports.

2.5 BUCKLE LENGTH AND DURATION DEPEND UPON MYOSIN-6 DENSITY

To test whether the separation along the actin filament affects the collective behaviors of myosin-6, I performed the FLIC assay at different myosin immobilization concentrations. The properties of buckles vary with myosin concentration (Figure 10). At increasing myosin concentrations, the buckles are shorter (as expected when increasing the surface density of myosins) and persist for shorter amount of time (Figure. 10A). This dataset can be divided into three empirical regimes (Figure 10*A,* color-coded). In the first regime, “single myosins,” less than one myosin per micron of a filament is expected (see Figure 8E). Under these conditions the buckles are rarely observed, because often only a single myosin is attached. In the “dynamic buckles” regime, the surface motor density varies from 1.2 – 3.1 myosins/μm actin, using values extrapolated from the density vs. concentration relation shown in Figure 8E. Many buckles of variable size are observed at these conditions. Finally, in the “micro-buckles” regime at the highest myosin density, the buckles become smaller and persist only briefly.

The distributions of buckle sizes for each immobilization concentration (excluding 5.2 nM where I do not observe frequent buckles) is shown in Figure 10B. To examine the dependence of buckle size on myosin density, the length and lifetime of the buckles was measured from the kymographs using a thresholding procedure (Figure 10*C*, see Materials and Methods). The distributions of buckle lengths shows that increasing myosin-6 immobilization concentration reduces the number of buckles over 1 μm. However there is no dramatic increase in the number of detected small buckles (< 0.5 μm) (Figure 10B), leading to overall decrease in a buckled area of a filament. This effect is consistent with the presence of a lower limit on a buckle length, below which the filament cannot be buckled or buckles are unstable and vanish. To test this hypothesis, I examined the dependence of the buckle lifetime on the buckle length (Figure 10D). The data presented here are pooled from all myosin concentrations except for 5.2 nM myosin-6. The trend in Figure 10D shows that buckle lifetime is shorter for the short buckles.

Buckles form when the trailing myosin (myosin B in Figure 9B) moves stochastically faster than the leading myosin (myosin C in Figure 9B). Buckles disappear when the leading myosin moves faster than trailing myosin to take up the slack in the filament, or through multiple other mechanisms involving myosin attachment and detachment. As I discuss below, the force transmitted through the filament may be high enough to couple the stepping behavior of the leading and trailing myosins, or it might be inconsequential, depending on the myosin spacing. Note that these situations are quite unlike the other alternative, where the actin segment between two myosins is under tension. Under tension, the leading myosin will quickly experience stall forces because it has no available actin to translate until the trailing myosin takes a step. Thus, if the tension is maintained, the two myosins must be either coordinated or stalled. This tension-based coordination is independent of the spacing between the myosins.

The critical force for the onset of buckling of an isotropic rod can be calculated using Euler equation, and is higher for short rods (see Materials and Methods). When the buckled segment of actin is short, the force can be sufficiently high to retard or stall the motion of the trailing myosin. A slower trailing myosin would allow the leading myosin to catch up and retract the buckle. This mode of coordination between the motors would lead to fast retraction of short buckles, but would not affect the long buckles. The force generated by long segments of actin is too low to impact the motor kinetics. Therefore, when the long segment of actin is buckled, it is equally likely that the buckle will be extended (when the trailing myosin B steps), as it is that it will be retracted (when the leading myosin C steps). Thus, long segments of buckled actin filaments decouple the myosins, while short buckled segments couple the myosins.

Notice that when we describe the plausible behavior of two neighboring motors I assume an asymmetrical response to the force generated by a buckle. This assumption is consistent with what is known for myosin-5, and perhaps all other processive myosins. For myosin-5, assisting force does not increase the forward stepping rate (Clemen et al., 2005; Gebhardt et al., 2006), while hindering force inhibits the myosin forward stepping rate (Clemen et al., 2005; Gebhardt et al., 2006; A. D. Mehta et al., 1999).

The alternative explanation of the trend in Figure 10D would claim that shorter buckles are formed by just one or two extra steps of the trailing motor (myosin B in Figure 9B), while the longer buckles are formed by more “missteps”. If this was the case, then load-independent stepping could rapidly retract the short buckles by chance alone, because only a few (possibly just 2) subsequent steps of the leading motor are required.

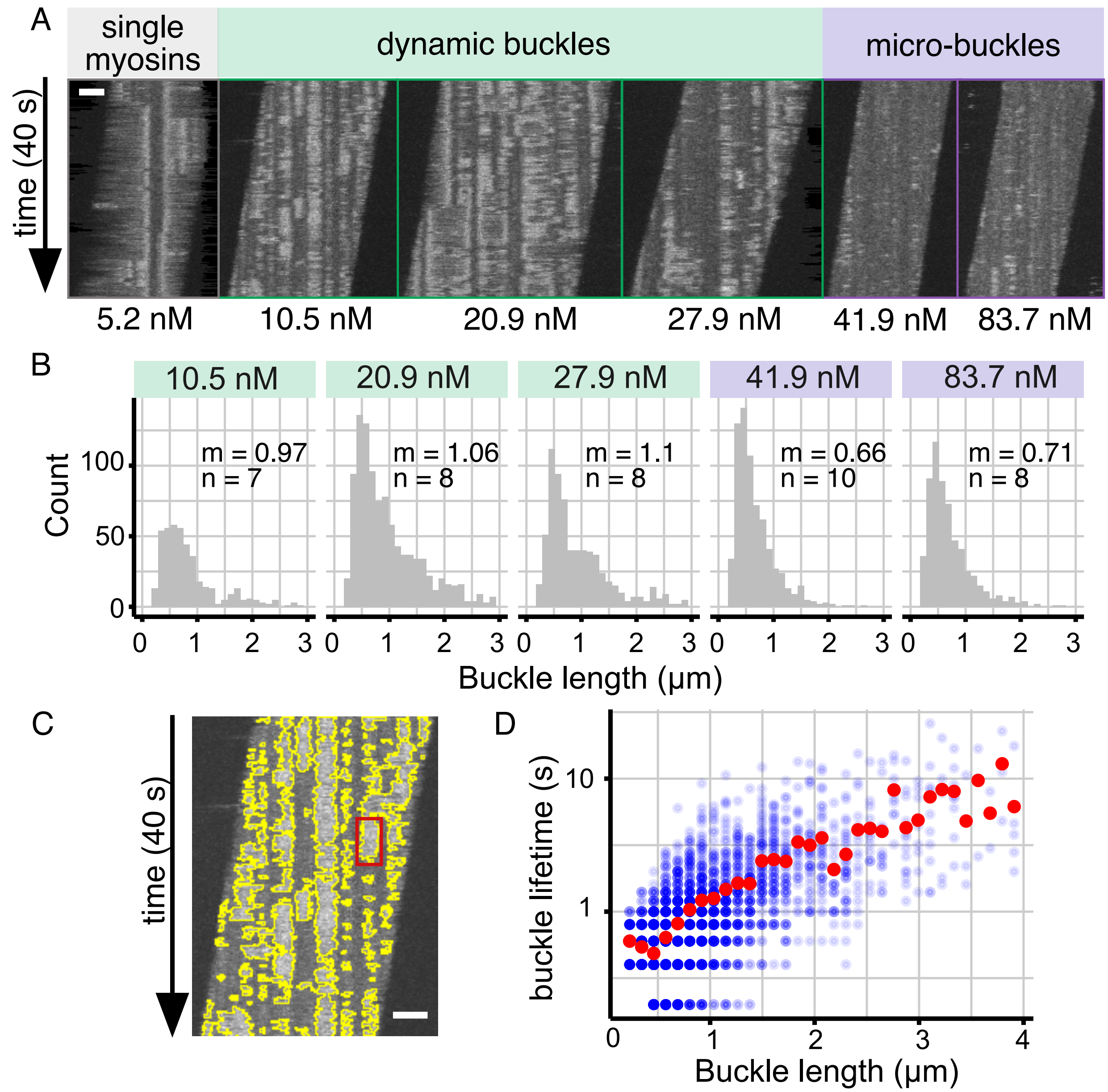

Figure 10. Actin filament buckling behavior depends on myosin surface density. (A) Buckles occur most robustly at intermediate myosin concentrations. The kymographs show an example filament at each myosin immobilization concentration. Three empirical regimes can be distinguished: single myosins, dynamic buckles, and micro-buckles. Scale bar, 3 *µ*m. (B) The distributions of buckle lengths show lower prevalence of very short buckles regardless of the myosin concentration. The histograms show the shift towards shorter buckles at increasing myosin concentration, however the number of detected 0.230 *µ*m long buckles is low across the entire dataset. Mean filament length: m, number of traced filaments: n. (C) Buckle lifetime and length measurements. The kymograph shows boundaries between buckled and non-buckled areas in yellow. Each buckle-containing area is then enclosed by a bounding box to determine the buckle lifetime and length (red box, see Materials and Methods).

Figure 10, continued. Scale bar, 3 μm. (D) The short buckles have a short buckle lifetime. Individual buckle lifetimes are plotted as a function of the buckle length (excluding the 5.2 nM dataset which had few buckles). The red dots show the mean buckle lifetime for every buckle length.

2.6 STOCHASTIC SIMULATION OF THE BUCKLE GROWTH AND RETRACTION PROCESS

To further understand the force-dependent coordination between the neighboring motors that enhances the fast retraction of short buckles, I performed stochastic simulations of a two-myosin ensemble using the Gillespie direct method(Gillespie, 1977). I ran the simulations for the three distances between the myosins, equivalent to buckle lengths, and compared the simulated results to the experimental data. The simulations were performed according to the model assuming force-dependent coordination (model 1) and unbiased stepping of myosins (model 2).

In model 1, the myosins take stochastic steps at rates determined by the forces produced by the middle segment of actin (Figure 11A). Forces are limited to tension, which switches off the leading myosin without affecting the trailing myosin, and compression, which affects the trailing myosin but not the leading. The upper limit of the compressive force experienced by the myosin is described by Euler's critical load for buckling.

In the model 1, two myosins are separated by a constant distance d, and they are allowed to step forward (Figure 11A). The stepping rate of the trailing myosin, which experiences the hindering force, is modulated according to the relationship described by Altman et. al (Altman et al., 2004) (from now on called Altman regulation) and depicted in Figure 11B. The leading myosin steps at its unloaded rate (k = 3.3 s^{-1}), unless the actin is pulled into tension when the length of actin segment between the two myosins is shorter than the distance between them. If the tension occurs, the leading myosin stalls, as the hindering force experienced by the motor would be above the stall force (Veigel et al., 1998).

To compare the simulated buckle lifetimes with my data, I set a threshold of 40 nm as a minimum height reached by the actin filament to be recognized as a buckle. To relate actin length to its height above the surface, I approximated the buckle length as an ellipse (see Materials and Methods). Although this profile is not accurate, especially at the surface tangent points, the ellipse contour length falls between those of a square profile and a triangular profile and is a reasonable approximation. At all three distances between the myosins investigated in Figure 11C, a single extra step of a back motor is enough to lift actin above the 40 nm threshold (see Materials and Methods) and produce a buckle that would be detected in a FLIC assay. Surprisingly, the majority of buckles observed in this dataset can be produced by a single myosin step.

Model 2 (unbiased stepping) is the same as model 1, except it does not include the Altman regulation of the forward stepping rate of the trailing myosin. Both myosins step at their unloaded rate, unless actin tension limits the leading myosin.

The 230 nm buckles are the shortest buckles I could detect in the FLIC assay. To ensure that I am not picking noise, I enforced the threshold condition of in our buckle-picking procedure. The buckle has to count at least 4 pixels to be recognized. For the 230 nm buckles it means that they have to persist for at least 0.4 s (2 frames) to be recognized. I applied the same lifetime filter to the simulation of 230 nm buckles. The 460 nm buckles are the most abundant buckles in my dataset. The distance between the myosins for 460 nm buckles is small enough to experience Altman regulation of the stepping rate. The 690 nm buckles represent the situation where the force exerted by the buckle is too low to modify myosin stepping rate, therefore model 1 and 2 give the same prediction.

For myosin separation of 230 nm and 460 nm, the distribution of attachment lifetimes is well approximated by model 1 and not model 2 (Figure 11C). The model 2 creates a wide distribution of attachment lifetimes, not observed in my data for short buckles. The good agreement between experimental data and simulations according to the model 1 for 230 nm and 460 nm buckles is a strong argument in favor of force-dependent step coordination between the motors at high myosin density. When the distance between the myosins increases, the force exerted by the buckle no longer plays a role in modulating the myosin stepping rate. I would expect a good agreement between the simulations according to model 2 and the experimental data at 690 nm buckle length. However, model 2 provided a moderately good approximation for the buckle lifetime at 690 nm myosin separation. There are two main reasons to which we can attribute the difference. I might be overestimating the buckle size, because of the buckle-picking procedure (each selection is enclosed by a rectangle) and the limitations of the microscopy (diffraction limited microscopy). Another reason would be the simplicity of the simulations, as neither of my models takes under the account events like myosin backstepping, detachments, or attachments of new myosins.

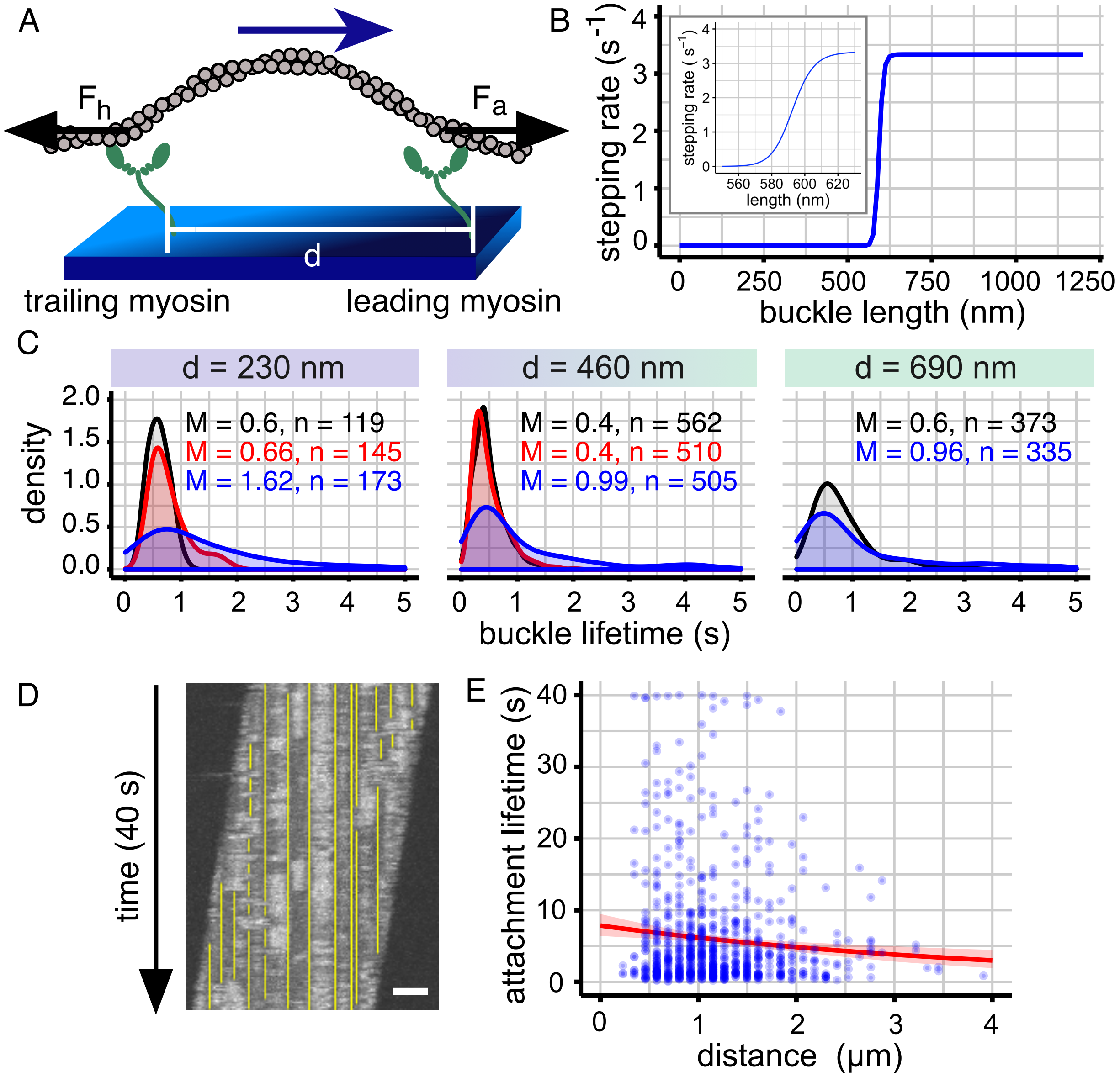

Figure 11. Force-based coordination mechanism limits the lifetime of short buckles and prolongs the myosin attachment lifetime. (A) Illustration of the simulation geometry. Two myosins are separated by a distance d, and are transporting an actin filament from left to right. The length of actin segment between the myosins is monitored throughout the simulation and used to determine periods of tension or compression. Hindering force, F_h; Assisting force, F_a. (B) The effect of buckling on the stepping rate of the left myosin, as a function of the buckle length. Stepping rates are given by Altman(Altman et al., 2004), at the critical load for a buckle of the indicated length. The inset shows the vicinity of the steep transition. (C) The simulation recreates the distribution of buckle lifetimes observed in the FLIC assay for small buckles. The full model (model 1, red) reproduces the experimental lifetime distributions (black) at 230 nm and 460 nm buckles. A limited model (model 2) that allows the left myosin to step at 3.3 s^{-1} independent of compressive forces (blue) has a broad distribution of buckle

Figure 11, continued. lifetimes. Median, M; number of observations, n. (D) Myosin attachment lifetimes. An example kymograph with manually selected myosin attachment lifetimes indicated (yellow lines). Scale bar, 3 μm. (E) Motors that have the close neighbors remain attached longer. The attachment lifetime data are fit to a Bell model exponential curve $\boldsymbol{T} = \boldsymbol{T_1} \boldsymbol{e}^{-\boldsymbol{distance}/\boldsymbol{\delta}}$, where T_1 = 7.85635 and δ =4.14921, by maximum likelihood estimation. The pink ribbon represents 95% confidence intervals obtained by bootstrapping 1000 datasets.

2.7 ENHANCED MYOSIN-6 RUN LENGTHS AT HIGH DENSITY

The hindering force leading to myosin coordination at high density may also have an effect on myosin attachment lifetime. To investigate this possibility I traced the attachment times of the individual myosins from the kymographs (Figure 11D), which allows me to express the lifetimes as a function of the distance to the nearest neighboring myosin (Figure 11E). The results show that myosins that have close neighbors stay attached for longer. This result is consistent with the previous work showing increased dwell time of myosin-6 at high load (Altman et al., 2004). Alternatively, it can be interpreted as an avidity effect of multiple motors holding actin at a distance optimal for sustained binding.

2.8 DISCUSSION

This work shows the application of FLIC microscopy for a study of collective myosin dynamics. In the FLIC assay, the location and attachment time of individual motors can be detected. I was able observe myosin-driven actin buckling or pulling to tension, and measure the magnitude of these actin deformations. The actin buckling is an indication of asynchronous myosin stepping. My data show that as the myosin concentration increases the buckles become smaller and less stable. The attachment lifetime of an individual myosin also increases with nearby neighboring myosins. These two results suggest a feedback mechanism leading to myosin coordination in a gliding filament assay. Closely spaced myosins coordinate their steps to minimize the internal strain between them. Coordination is the strongest when myosins are sufficiently close, which increases the critical force required to buckle the actin filament. These results show that the mechanical coupling through actin filament regulates the collective myosin-6 behavior.

In many reports investigating the multi-motor dynamics of unconventional myosins, the myosins are linked by a quantum dot (Ali et al., 2011), DNA scaffold (Lu et al., 2012), or a vesicle (Nelson et al., 2014), and they walk along surface-immobilized filament in a Total Internal Reflection (TIRF) assay. The TIRF assay enables the observation of states of the individual, labeled motors (Ali et al., 2011; Lu et al., 2012) and mimics many aspects of cargo transport. However, the TIRF assay allows for only limited observation of actin deformation and, depending on exact experimental conditions, any actin shape variation might be severely constrained. Therefore I believe that the FLIC assay could serve as a complementary approach. It allows me to observe the dynamics of the actin filament under the influence of a fixed complement of myosin motors, which can be localized and identified as bound or detached from the actin filament.

In vitro, negative cooperativity, as observed by a reduced velocity and/or attenuated run length of a motor complex (relative to the model assuming no interaction between the motors), has been proposed for other processive motors including myosin 5 (Berger et al., 2012; Lu et al., 2012; Rogers et al., 2009). In my assay, I observe an increased attachment lifetime of an individual myosin if another myosin is in its vicinity (Figure 11E). This response is consistent with increased dwell time of myosin-6 when external loads are applied (Altman et al., 2004), however, it is unclear to what extent this effect depends upon the experimental geometry.

In a FLIC assay, myosins are mechanically coupled through the actin filament. It is expected that the elastic properties of F-actin (e.g., the persistence length, L_p, used to calculate the Euler force) play crucial role in modulating the behavior of the myosin ensemble. The role of filament elasticity is in agreement with previous reports, which found that the behavior of a motor assembly depends upon the properties of the motors and the connections between them (Berger et al., 2012; Kohler and Rohrbach, 2015; Lu et al., 2012; Nelson et al., 2014).

The data presented here show robust actin buckling at the intermediate concentrations of myosin-6. Actin buckling powered by myosin II is crucial for symmetry breaking between tensile and contractile forces, which is necessary to drive network contraction in a minimal model of the cell actomyosin cortex (Murrell et al., 2015; Murrell and Gardel, 2012). I speculate that myosin-6 motors attached to a large cellular structures that provide the necessary separation, like the Golgi apparatus or the plasma membrane between the sterocillia (Frank et al., 2004; Self et al., 1999; Warner et al., 2003), could buckle a segment of actin between them. However, the force transmitted between the myosins in this scenario is expected to be low and insufficient to lead to the coordination of myosin stepping. Additionally, membrane fluidity would play role in modulating the extent of myosin-6-driven actin deformation. On the other hand, when myosin-6 transports smaller objects like clathrin-coated vesicles that are only 100 – 150 nm in diameter (Buss et al., 2001), the myosins would be mechanically coupled through the filament. If the buckling occurred between the myosin-6s attached to endocytic vesicles, it would still transmit a high force between the myosins and would lead to myosin coordination. The buckling could relax the normal force experienced by the myosin-6s attached to the curved vesicle.

The study of myosin-6 collective behavior presented here shows the unique utility of the FLIC assay to investigate the acto-myosin interaction. However there are still many questions that remain to be addressed. Apart from coordination of a forward step between neighboring motors, does the decreased buckling at high myosin concentration (see Figure 10A) indicate “lock-step” type of synchronization between myosins? Such synchronization between motors has recently been proposed as a possible mode of motor cooperation (Kohler and Rohrbach, 2015). Moreover, how do different myosin classes behave in a FLIC assay? These and many other questions should be the subject of future studies.

CHAPTER 3: FLIC STUDY OF OTHER PROCESIVE MOTORS

FLIC microscopy is a versatile technique that can be used to study different classes of myosins. The technique can be used to study processive and non-procesive motors; therefore, it allows for observation of a broad range of myosin behaviors.

This chapter presents preliminary data showing the behavior of myosin-5 and NMIIB in a FLIC assay. Both of these motors are processive, however, NMIIB takes only few 5.5 nm steps along the actin (average runlength is ~12 nm) (Norstrom et al., 2010). Both myosins characterized in this chapter appear very different from each other in a FLIC assay. The implication of these differences and how they contribute to our understanding of myosin function are discussed at the end of the chapter.

3.1 MYOSIN-5 MORORS STEP ASYNCHRONOUSLY DURING ACTIN TRANSLOCATION.

Myosin-5 is responsible for organelle and vesicle transport inside a cell (Hammer and Sellers, 2012). In vitro, a single myosin-5 dimer can take a micrometers-long walk along the actin track (A. D. Mehta et al., 1999; Zimmermann et al., 2015). This behavior, together with the relative ease of myosin preparation (does not need artificial dimerization domain, easier to purify than many other myosins) has made myosin-5 the “workhorse” of the single molecule studies.

In a FLIC assay, the locations of myosin-5 motors are clearly visible when actin is gliding over the surface (Figure 12A and B). The single field of view can reveal thousands of myosins (Figure 12A). The protein preparation quality can be directly evaluated by counting the ratio of damaged and nonmotile myosins to active myosins (here 99.1% active motors). The majority of myosins appear as short 345 - 575 nm segments of actin (Figure 12B and C), corresponding to 3-5 pixels. Apart from myosin binding, FLIC reveals events like plectoneme formation and resolution (a "plectoneme" is a twisted loop in a string, Figure 12B, the filament marked in red arrows). Because the fluorescence intensity contains the information about the distance to the surface, it is obvious from the movie that the "actin loop" has a left-hand twist. This handedness means that if the strand of actin is oriented so that the barbed end goes up, the left hand approximates which way the strand curves, with the thumb pointing up and fingers going to the left. Note that the barbed end of actin is the trailing end of actin where propelled by myosin-5. The left-handed single twist of actin must be caused by the right-handed torque imposed to the actin filament by the myosin-5. This is unexpected because the single unloaded myosin-5 spirals towards the left on the actin filament (Ali et al., 2002). The right-handed torque is interpreted as an effect of collective behavior of myosins, and its mechanistic origin (e.g. prolonged or shortened step size) should be further explored.

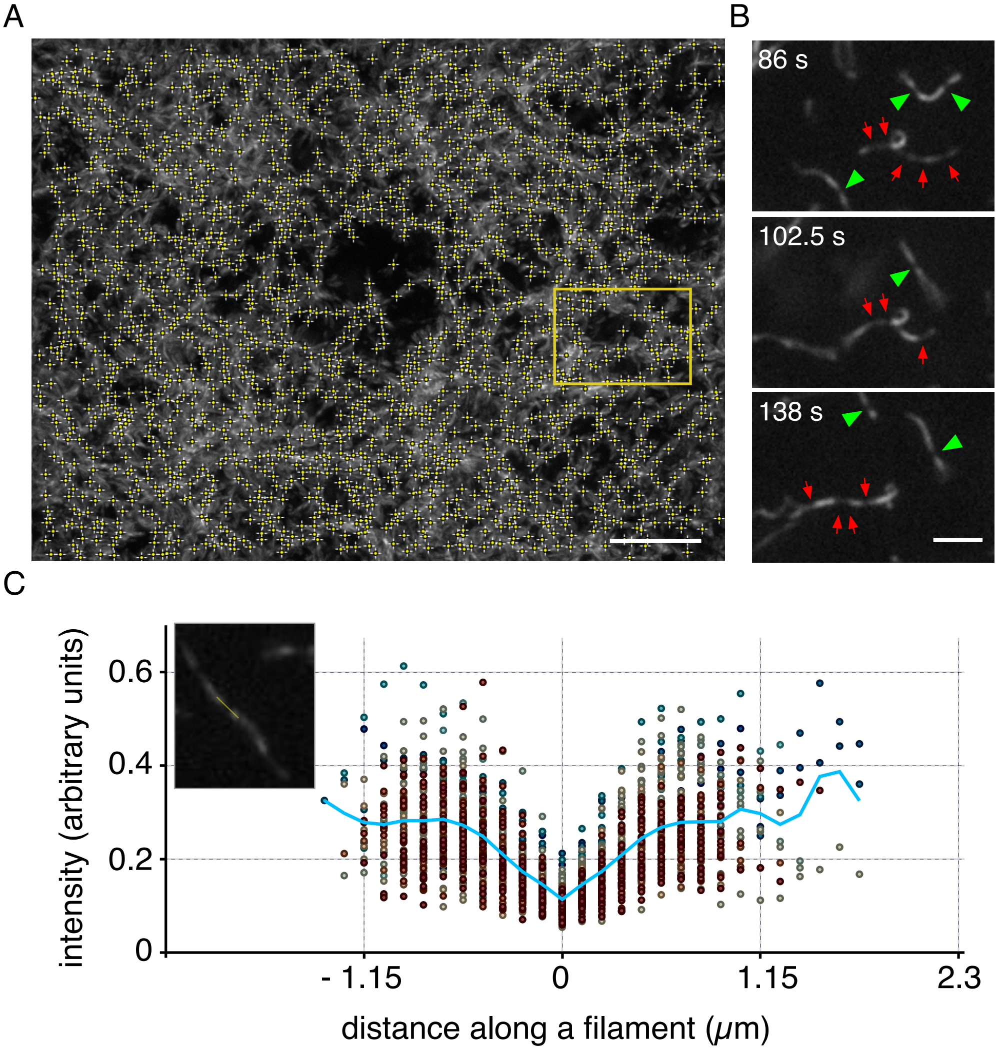

Figure 12. Myosin-5 appears as a dim segment of actin in a FLIC assay. (A) Maximum intensity projection of a movie where 1918 myosin-5s were marked (crosses). Scale bar 10 μm (B) Enlarged section of a field of view as marked in A. Myosin attachments are marked (red arrows and green arrow heads). Red arrows mark a filament forming a plectoneme. Scale bar 3 μm. (C) The fluorescence intensity profile of 121 actin segments with myosin attachment present in the middle (the profiles were aligned to their darkest pixel). The inset presents an example of a single selection and the blue line is an average intensity at each point. The V-shape of the plot is a consequence of the alignment process. The majority of myosin-5s appeared as dark spots of 3-5 pixels long (1 pixel = 115 nm). It can be seen in the graph, as the distribution of the pixel values at the 3 dimmest points is tighter than at the other positions.

The time the myosin remains visible in a FLIC assay can be used to calculate myosin attachment time. The preliminary measurement of attachment lifetime for single myosin-5 (transporting actin filament in a single molecule configuration) yields a median lifetime τ = 11 s (Figure 13). This value translates to ~1 μm long runlength (RL). The runlength reported here might be an underestimate, because it was obtained by multiplication of the attachment lifetimetime and the average gliding velocity in the assay (V =93 nm/s, S.D = 12.4 nm/s). However, other reported runlengths are close in the magnitude (RL = 790 nm in TIRF assay (Zimmermann et al., 2015) and RL = 1.6 μm in landing assay (A. D. Mehta et al., 1999)).

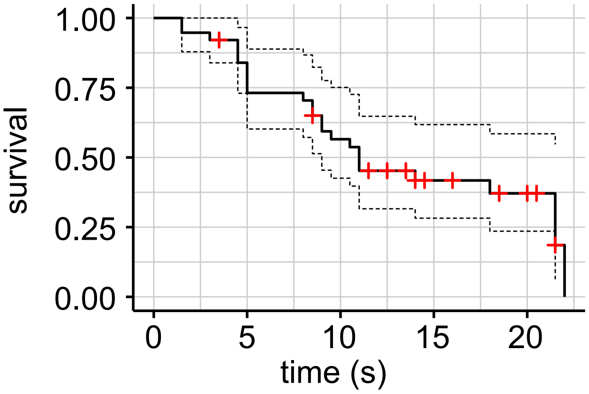

Figure 13. Attachment lifetime of a single myosin-5 can be measured in a FLIC assay. The attachment lifetime of myosin-5 transporting actin in a single motor configuration was measured from the movie. The survival analysis gives the median lifetime τ = 11 s. Crosses indicate the right-censored data points. Doted lines show high and low 95% confidence intervals (CI_{low} = 9, CI_{high} = NA). The dataset included 38 data points.

As in case of myosin-6, myosin-5 deforms the actin filament during translocation. A short sequence of images showing myosin-5-driven actin deformation is presented in Figure 14. As the myosin-5s step asynchronously, they pull actin into tension (Figure 14, red arrowheads) or buckle it (Figure 14, yellow arrows). The buckled segments of actin are brighter, as they project away from the surface. The segments of actin under tension appear dim, as they are pulled closer to the surface (Figure 14).

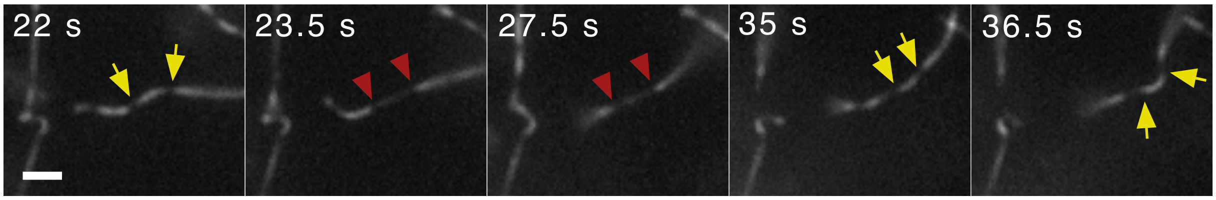

Figure 14. Asynchronous myosin-5 stepping causes actin deformation. Frames showing the progression of a single actin filament pulled by myosin-5. Yellow arrows mark ends of actin segments buckled away from the surface between two engaged myosin-5 s. Red arrows mark ends of a segment of actin pulled into tension between two motors, and therefore pulled closer to the surface. Scale bar, 3 μm.

The transition between buckled, stretched or relaxed segment of actin is a dynamic process, which takes place only in presence of ATP (Figure 15), meaning it requires an active myosin. When myosin-5 is immobilized at 20.6 nM concentration and imaged in the absence of ATP (Figure 15B), the filaments appear static and uniform in fluorescence. However, when ATP is present in the flow cell, the filaments glide (they are gradually moving to the left) and the dynamic pattern of bright and dim fluorescence appears (Figure 15A). The straight, vertical, non-translocating lines of low fluorescence intensity identify myosin attachments. They are clearly visible in the kymographs and can be selected to obtain myosin-5 attachment lifetimes.

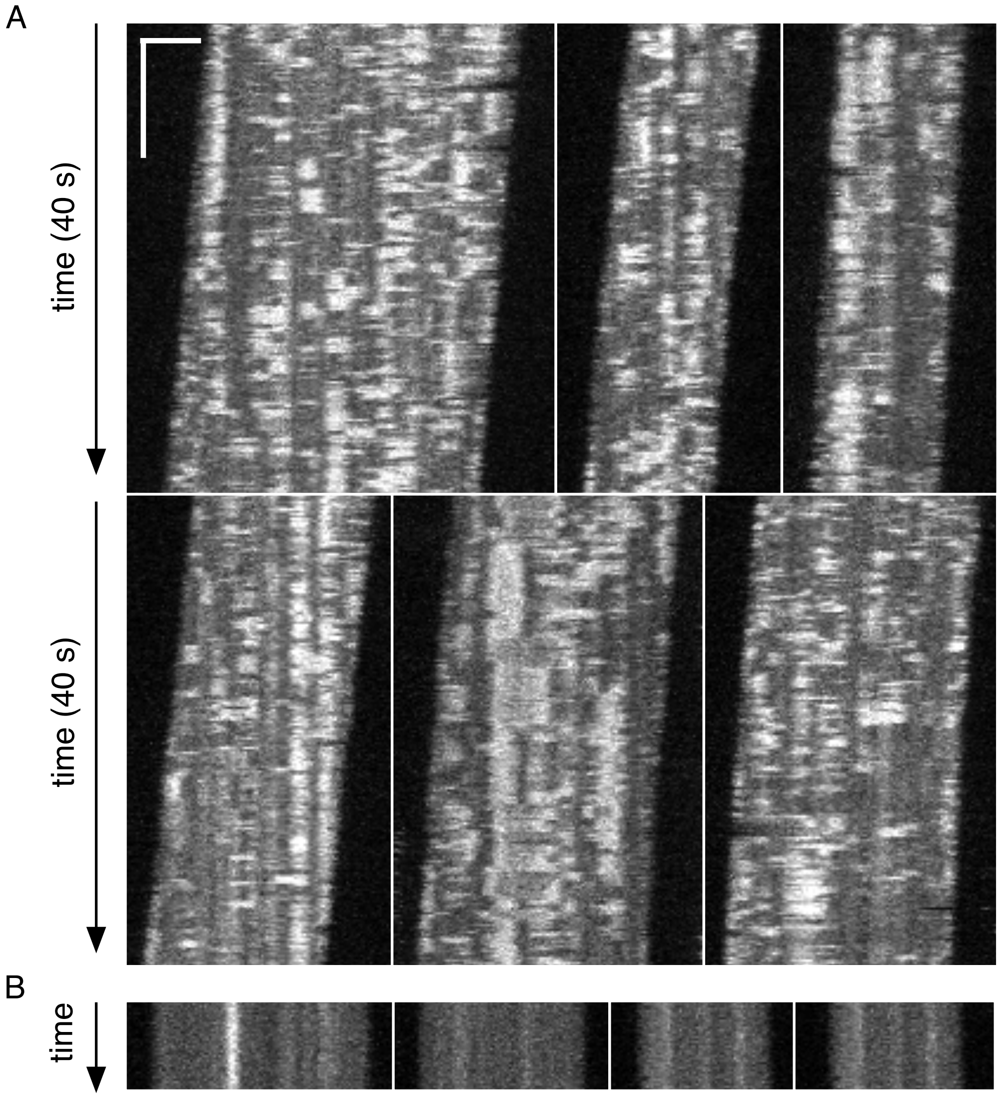

Figure 15. The dynamic actin deformation occurs in the presence of ATP. (A) Filaments pulled by myosin-5 at 2 mM ATP. Myosin-5 was immobilized at 20.6 nM concentration. The filaments are gliding and therefore they shift to the left in the kymographs. The vertical lines of dim fluorescence are myosin-5 attachments. The segments between them are frequently buckled. (B) The filaments from the same wafer, imaged in the absence of ATP. The filaments are static and appear a lot more uniform in their fluorescence than in A. Each kymograph represents 7.6 s window of observation. Scale bar 10 s (vertical), 3 μm (horizontal).

The preliminary analysis of buckle properties (at 20.6 nM myosin-5) reveals that the median buckle size is 0.805 μm and the median lifetime is 0.8 s. The distribution of buckle lifetime as a function of buckle length seems to follow the same trend as for myosin-6 (Figure 16), where the short buckles are more likely to have a short lifetime.

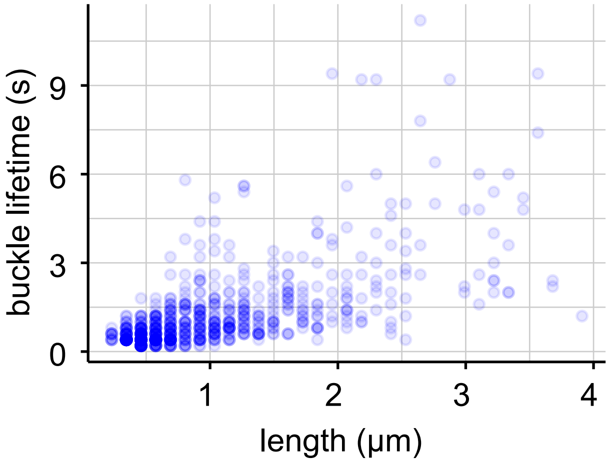

Figure 16. The lifetime of myosin-5 induced buckles as a function of buckle length. The buckles were selected from 10 filaments, pulled by myosin-5 (20.6 nM immobilization concentration). The distribution of buckles shows that shorter buckles persist for shorter amount of time.

3.2 THE INTERFERENCE OF MOTORS INCREASES THE ATTACHMENT LIFETIME OF NMIIB

NMIIB is a molecular motor responsible for cytoskeleton tension maintenance inside a cell (Morano et al., 2000; Rhee et al., 2006). Here, the activity of dimeric NMIIB HMM myosin is tested in a FLIC assay.

NMIIB can take a short processive walk along the actin filament (average RL = 12 nm, reported by Norstrom et. al (Norstrom et al., 2010)). Because the processive runlegth of NMIIB is very short, the concentration of the motor required to support the gliding of filaments is higher than for myosin-5 and myosin-6. This in turn affects the appearance of the filaments in the assay. At high myosin concentration (~ 2 μM) the filaments appear almost uniform in fluorescence (data not shown) in a FLIC assay. As the myosin concentration is reduced to about 500 nM, the dynamic pattern of bright and dim fluorescence emerges in the traced filaments (Figure 17). At this concentration, which is ~6 times higher than the highest concentration used for myosin-6 studies, the gliding is smooth and uninterrupted. The average gliding velocity is 30.6 nm/s (SD = 1.7 nm/s), as previously reported (Norstrom et al., 2010). However, it is impossible to localize the individual myosins at these conditions. The 2-fold dilution in myosin concentration leads to a dramatic decrease in the number of filaments present at the surface and lower velocity (data not shown). The velocity is in a range of 4 nm/s to 18 nm/s and can be measured directly from a kymograph – by measuring the angle the filament end forms with the normal. The few filaments that could be traced and analyzed are shown in Figure 17B. Notice that the pattern of actin deformations at 263 nM NMIIB reveals long attachments (Figure 17B, dark, vertical lines). These attachments have sharp edges on both sides (they are not blurry as the buckle edges in 17A) and their overall appearance resembles the single myosin attachments as seen in Figure 15A or Figure 11D.

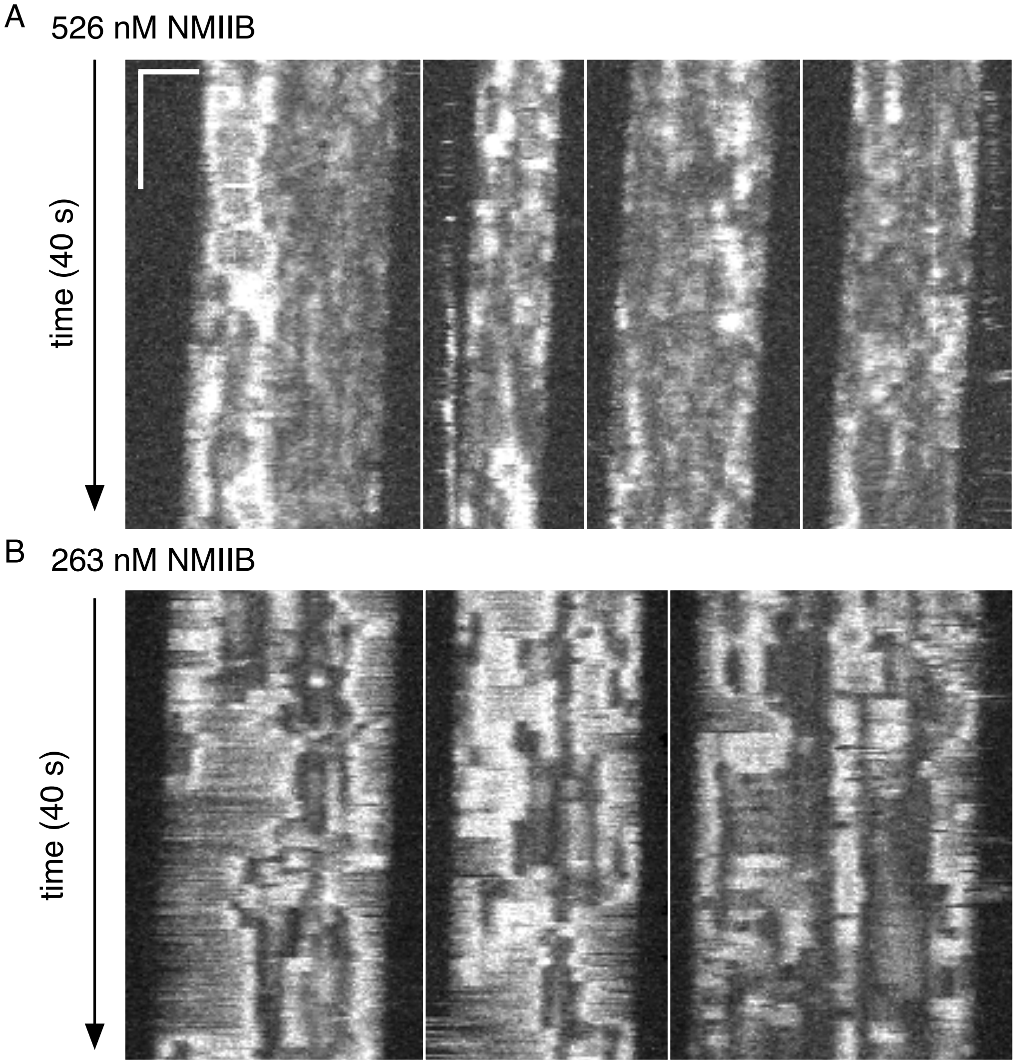

Figure 17. NMIIB buckles actin at much high myosin concentration. (A) Filaments pulled by NMIIB at 2 mM ATP. NMIIB was immobilized at 526 nM concentration. The filaments are gliding and therefore they shift to the left in the kymographs. Although actin buckling is visible in the kymographs, the individual attachments cannot be resolved at this motor density. (B) NMIIB was immobilized at 263 nM concentration. The filaments move slower, however the attachments, resembling single molecule attachments, can be observed. Scale bar 10 s (vertical), 3 *μ*m (horizontal).

The attachment lifetimes were measured from the kymographs of 263 nM NMIIB (Figure 17 B). From just 3 filaments 93 individual attachments were selected, as shown in Figure 18A. The survival analysis of these attachments revealed that the median lifetime was $\tau = 2.4$ s (Figure 18B). This value is higher than the attachment lifetime calculated from the single molecule optical tweezers measurements (τ = 1.1 s) (Norstrom et al., 2010), however it is on the same order of magnitude. The nature of these attachments (are they a single, double, triple-motor attachments?) should be a subject of further investigation. If these are multi-myosin attachments, what can we learn about the interaction between NMIIB myosins from them?

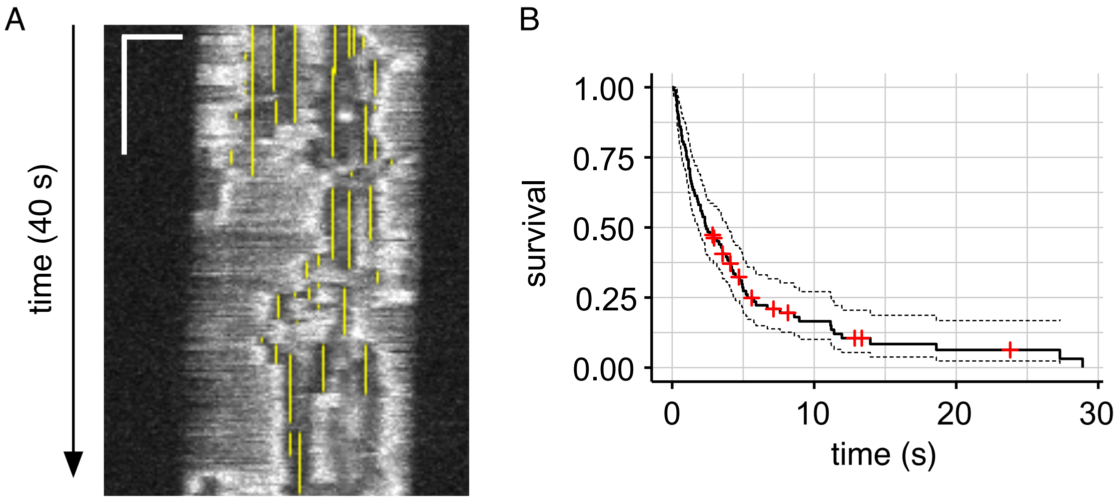

Figure 18. The NMIIB attachment lifetime measurements. (A) The attachment lifetimes are selected from the kymographs. The length of the yellow line indicates the time myosin(s) is/are bound to actin. Scale bar 10 s (vertical), 3 *μ*m (horizontal). (B) The survival analysis of attachment lifetimes (n = 93). The survival analysis gives the median lifetime τ = 2.4 s. Crosses indicate the right-censored data points. Doted lines show high and low 95% confidence intervals (CI_{low} = 1.8 s, CI_{high} = 3.9).

3.3. CONCLUSIONS

The data presented in this chapter highlight the difference between highly processive and marginally processive myosins. The single molecule behavior of myosin-5 can be studied in the FLIC assay. The values of attachment lifetime and gliding velocity can be obtained for the individual myosin-5s transporting actin as a single motor and as part of myosin ensemble. The qualitative comparison between myosin-5 and myosin-6 reveals no obvious differences between these motors. Myosin-5 steps asynchronously when immobilized to the surface at intermediate protein concentration. Actin buckling or stretching, and plectoneme formation are signs of asynchronous stepping of myosin-5. The short buckles are more likely to be rapidly retracted, similar to what I have shown for myosin-6.

On the other hand, NMIIB behaves very differently in a FLIC assay. Due to the low processivity of NMIIB, the dynamic range of myosin concentration over which the data can be collected is smaller. The gliding velocity is lower at low NMIIB concentration (Figure 17B), although the nature of this trend is unclear. It is possible that at these conditions where very little actin is pulled down, only the impaired motors retain actin for long enough to be imaged. However the filaments presented in Figure 17B show the detachment events of most of the motors and no signatures of a dead myosin (e.g. growing buckle behind a myosin or a segment of actin constantly under tension). In fact, decreased velocity of NMIIB at low concentration is consistent with the data on skeletal and smooth muscle myosin. At high motor concentration, skeletal and smooth muscle myosin display higher velocity in gliding filament assay (Uyeda et al., 1990; Walcott et al., 2012). Walcott and colleagues attribute this observation to the internal forces experienced by the myosins during collective transport. These forces would increase the ADP release rate (decreasing the attachment lifetime) and increase a unitary step of myosin (Walcott et al., 2012). However, skeletal and smooth muscle myosins are low duty ratio motors, therefore the increase in number of available motor heads (that could provide the assisting load for their neighbors) is expected to have a dramatic effect on ensemble behavior. It is unclear whether NMIIB would be similarly affected.

Alternatively, the velocity measured by tracing the edge of actin filament might be deceiving as the pulled segment of actin can be buckled instead of translated horizontally. This effect would introduce a higher proportional bias for the velocity measurements of the slow myosin (like NMIIB) than the faster myosins (e.g. myosin-5 and myosin-6).

Taking into account this ambiguity, it is difficult to interpret the long attachment lifetime of NMIIB measured in a FLIC assay (τ_{FLIC} = 2.4 s versus $\tau_{tweezers}$ = 1.1 s). These attachments resemble a single molecule attachments (sharp edges, large spacing between them), and the prolonged lifetime of a single motor can be reconciled with lower velocity of an ensemble (negative "cooperation"). However, based on the concentration versus myosin density relationship obtained for myosin-6 (Figure 8E), it seems unlikely that these attachments represent single molecule binding. The nature of these binding events should be further investigated.

In a summary of this chapter, I conclude that both highly processive and marginally processive myosins can be studied in the FLIC assay. Although the results obtained for NMIIB are at present difficult to interpret, they represent a good starting point for future investigations.

CHAPTER 4: CONCLUDING REMARKS AND FUTURE DIRECTIONS

The research presented in this thesis describes the novel application of FLIC microscopy for the studies of collective myosin dynamics. Due to the unique properties of the acto-myosin network, FILC can be used to simultaneously observe the behavior of the individual myosins and the behavior of the myosin ensemble. The technique is easy to perform and versatile. It was successfully used here to study highly processive motors (myosin-5 and myosin-6) and marginally processive motors (NMIIB).

The FLIC assay reveals the unappreciated aspect of acto-myosin interaction. Actin buckling is very extensive in gliding filament assay geometry. It points towards the modulation of force transduction through the actin filament for collective myosin functions. This aspect of ensemble dynamics was not explored in previous studies of myosin cooperativity. However, there is a growing number of evidence highlighting the importance of myosin-driven actin buckling for cell function (Murrell et al., 2015).

4.1 FLIC IS AN ENSEMBLE TECHNIQUE WITH A SINGLE MOLECULE CAPABILITY

The studies of acto-myosin network require multiple complementary approaches, to tackle the complexity of this system. Single molecule methods provide a qualitative and quantitative description of myosin properties. However, relating the cellular processes (like mitosis, cell migration, intracellular transport etc.) to the properties of the individual molecular motors remains challenging. Therefore, there is a need for the techniques that can bridge the gap between the single molecule experiments and whole cell experiments.

The FLIC assay straddles in the middle between single molecule and ensemble methods. The assay allows us to observe the actin transport carried out by multiple motors with simultaneous insight into the engagement status of each motor. Therefore, to a certain extent the FLIC assay mimics the capabilities of TIRF assay and optical tweezers. Here, FLIC is compared with these two single molecule methods for selected applications. However, it needs to be emphasized that although FLIC enables the simultaneous observation of the individual motors and ensemble dynamics, there is a trade off between these two applications. High myosin density is usually more desirable in the studies of myosin collective behaviors. However, increasing the motor density increases the chance of misidentifying a double-myosin attachment as a single myosin.

4.1.1 SINGLE MOLECULE ATACHMENT LIFETIME AND POSITION ASSIGNMENT

In FLIC, the position of myosin is detected when the segment of actin directly above it becomes darker. The actin appears darker because the myosin attachment brings it closer to the reflective surface, where the destructive interference dominates. Unlike in TIRF, the myosins are not fluorescently labeled in FLIC, however they are surface immobilized.

Although at present FLIC allows for location assignment of a myosin with a limited precision (diffraction limited microscopy) the further development of image processing algorithms should greatly improve it. Fitting the filament shape to the theoretical models based on Gaussian distributions, as it was done in filament tracking software FIESTA (Fluorescence Image Evaluation Software for Tracking and Analysis) could be the first step

(Ruhnow et al., 2011). The centerline and tips of microtubules traced with FIESTA were described with the precision of ~2 nm and ~9 nm, respectively. This or similar procedure would provide a good starting point towards improving the spatial resolution of FLIC. However, the FLIC-specific algorithm has to take into account the large fluctuations in fluorescence intensity and their implications for the model of filament shape. With future advances, it is possible that FLIC could be developed into a method matching TIRF in its spatial resolution.

In terms of temporal resolution, as in case of TIRF microscopy, there is a tradeoff between spatial and temporal resolution. As the frame rate increases the number of detected photons per frame decreases. For FLIC it would translate to a lower precision of the height assignment. Depending on the specific application of FLIC the frame rate can be adjusted to obtain a desired spatial/temporal resolution. Here, the FLIC images were obtained with the lowest acquisition time of 200 ms (frame rate 5 s^{-1}). This allowed us to observe clearly defined buckles and attachment spots. However, the frame rate of 10 s^{-1} was used with FLIC to resolve the pitch of kinesin-1-induced microtubule rotation (Nitzsche et al., 2008). With a use of brighter fluorophores with higher quantum yields, the images could be obtained at even higher frame rate.

In contrast to TIRF assay, which is suitable mainly for the studies of highly processive myosins, the FLIC assay can be used to study marginally processive myosins too. Here, the pilot experiment showing the attachment lifetime of NMIIB is shown. The attachment lifetimes of hundered milisecond time scales were detected in FLIC. These correspond to runlengths shorter than 20 nm. This measurement would be very difficult and frustrating in a TIRF assay beacause it would be hard to distinguish between the fluorophore just hitting the actin versus the short processive runs. Therefore, I believe that FLIC can be developed into simple and reliable tool allowing for measurements of single molecule properties (e.g. runlength/attachment lifetime) of marginally processive or even non-processive myosins.

4.1.2 ACTIN SHAPE DESCRIPTION AND FORCE MEASUREMENTS

The position of a fluorophore can be assigned in three dimensions using FLIC microscopy (Kerssemakers et al., 2006; Lambacher and Fromherz, 1996). I believe that the complete description of actin shape will allow for reliable force measurements using FLIC microscopy. In chapter 2, I presented a simple example of how the force measurements cam be performed and used in FLIC. By calculating the critical force for buckling, for a filament of a given length, I approximated the force that the myosins experience in the assay. Based on that, I calculated the force-sensitive rate of forward steps for the trailing myosin. Further advancement, like better shape description leading towards more reliable force calculation, could transform the FLIC microscopy into an alternative for optical tweezers for force-sensitive measurements. The advantage of FLIC over optical tweezers would be the simplicity of the experimental set-up and quantitative robustness, in that a single field of view may contain thousands of myosins.

4.2 MYOSIN COUPLING THROUGH THE ACTIN FILAMENT – IMPLICATIONS TO INTRACELLULAR TRANSPORT

The collective motor dynamics of processive myosins is predominantly studied in the TIRF assay (Ali et al., 2011; Lu et al., 2012; Nelson et al., 2014). In the TIRF geometry, like the experimental designs shown in Figure 5, the actin track is immobilized to the surface and a team of elastically coupled myosins walks on top of it. The general rules of collective motor behaviors have been derived for these assays. However, the actin filament is treated as a rigid rod in these models (Ali et al., 2011; Berger et al., 2012; Kohler and Rohrbach, 2015; Lu et al., 2012; Nelson et al., 2014). Also the tethering of actin to the surface of a slide might influence the flexibility of actin. The role of a filament for regulation of coupling between the myosins has not been explored in the context of processive motors. Inside a cell, myosins perform a variety of functions, directing them to distinct actin networks (Blanchoin et al., 2014). Thus, actin flexibility might be an important element influencing collective myosin behavior.

In FLIC assay the myosins are mechanically coupled through the actin filament. The state of actin between two attached myosins can be assigned to either of two categories: buckled or under tension. The results presented here show that actin buckling is a measure of mis-synchronization between the motors. The relationship between buckle lifetime and buckle length suggests that, depending on myosin spacing, actin can act either as a force transducer or as a compliant element. As shown here, this result can have important implications to our understanding of intracellular transport of cargo.

Inside a cell, myosins can transport the cargo of different size. Clathrin-coated vesicles are ~100 nm in diameter (Buss et al., 2001) , while other organelles like the ER or Golgi can be micrometers long (Tabb et al., 1998; Warner et al., 2003). Although the larger cargo is usually associated with higher number of motors (Tabb et al., 1998), the position of these motors on the cargo and availability of actin tracks may lead to different spacing between the motors for small versus large cargo. If two myosins are far apart from each other and they walk along the same actin track, it is possible that the segment of actin between them would act as a compliant element and the motors would be un-coordinated. If the segment of actin between the motors is short, the actin segment will be stiff and the myosins would be coordinated. Of course the properties of the cargo like membrane fluidity and vesicle curvaturure (Nelson et al., 2014) would affect the intracellular transport as well. One expectation is that the filament buckling would reduce the force normal to the actin axis, which in turn could result in longer processive runs of the myosins. The nature of the connection between the cargo and the motor would be another sources of compliance in the system. The mechanical coupling between the processive motors modulates the velocity of the complex (Kohler and Rohrbach, 2015; Lu et al., 2012), therefore it is expected to impact the intracellular transport.

The coordination of steps between the coupled myosins has been shown for linked oppositely directed motors (myosin-5 linked to myosin-6) walking along a surface immobilized track (Ali et al., 2011). In this report, one of the motors wins (usually myosin-5), forcing the other myosin to continuously step backwards while maintaining the motor specific step size. These studies demonstrate that the internal load between the linked motors can be high enough to induce backsteping. The authors suggest that the competition between oppositely directed motors would be very important for cargo trafficking. How would actin flexibility regulate this interaction if the spacing between myosins was sufficiently long (here the motors were conjugated to a small quantum dot) and the actin was not immobilized to the surface? How would the competition between the myosins look in a FLIC assay? Would it lead to long, growing buckles or segments under tension depending on the orientation of actin filament between the myosins? Or would one of the motors dominate the actin transport? An actin polarity marker (e.g., fluorescently labeled formin or capping protein) and/or myosin labeling can be used to facilitate the interpretation of the results.

4.3 BUCKLING OF THE ACTIN CYTOSKELETON

Although actin buckling *in vivo* might seem counter-intuitive at first, especially when considering that one of the roles of cytoskeleton is to sense and respond to external forces (Luo et al., 2013; Schwarz and Gardel, 2012), actin buckling seem to be crucial for network contractility *in vitro* (Murrell et al., 2015; Murrell and Gardel, 2012). In a minimal model of the actomyosin network, the force generated by myosin II caused extensive buckling of the filaments, driving network contraction. Network contraction strain of up to 80% could be assigned to the buckling. The buckling is a consequence of low resistance of F-actin to compressive forces (bends at ~ 1 pN forces). For comparison F-actin can resist up to ~ 300 pN and tensile stress. This non-linear response of actin to stress was proposed as a mechanism for breaking the symmetry between contractile and extensile forces which is necessary for contraction to occur in the networks lacking the sarcomere-like organization (Murrell et al., 2015; Murrell and Gardel, 2012). Whether or not the intracellular traffic and organelle positioning can additionally contribute to the contractility of actin cytoskeleton could be a subject of future investigation.

4.4 FUTURE DIRECTIONS

There are several future directions that are stemming from the work presented here. Among them, the question of preference of different myosins and actin binding proteins for segments of actin either under tension or compression. The structure and properties of actin bundles could be also explored in the FLIC assay.

4.4.1 THE PREFERENCE OF PROCESSIVE MYOSINS FOR ACTIN IN DIFFERENT STATES

Inside a cell, the processive motors may encounter the variety of actin tracks, differing in their biophysical properties. Myosin-10 for instance has been shown to prefer actin-bundles than single filaments for its tracks (Nagy et al., 2008). Myosin-5 has longer processive runs along young (ADP-Pi) actin than old (ADP) actin, while myosin-6 prefers the opposite (Zimmermann et al., 2015). It would be interesting to see if myosins have a preference for actin under tension versus compression. The FLIC assay, set up in the standard way with myosins immobilized to the surface and labeled actin gliding, but with addition of a low concentration of quantum dot-labeled myosin (QD-myosin) in solution, would help to answer this question, as illustrated in Figure 19A. It is expected that QD-myosin would land on moving actin and start walking. We would expect the increased detachment frequency when the motor passing through the segment of actin in its disfavored state, either under compression or tension. The landing rate can be also different for compressed versus tensed actin.

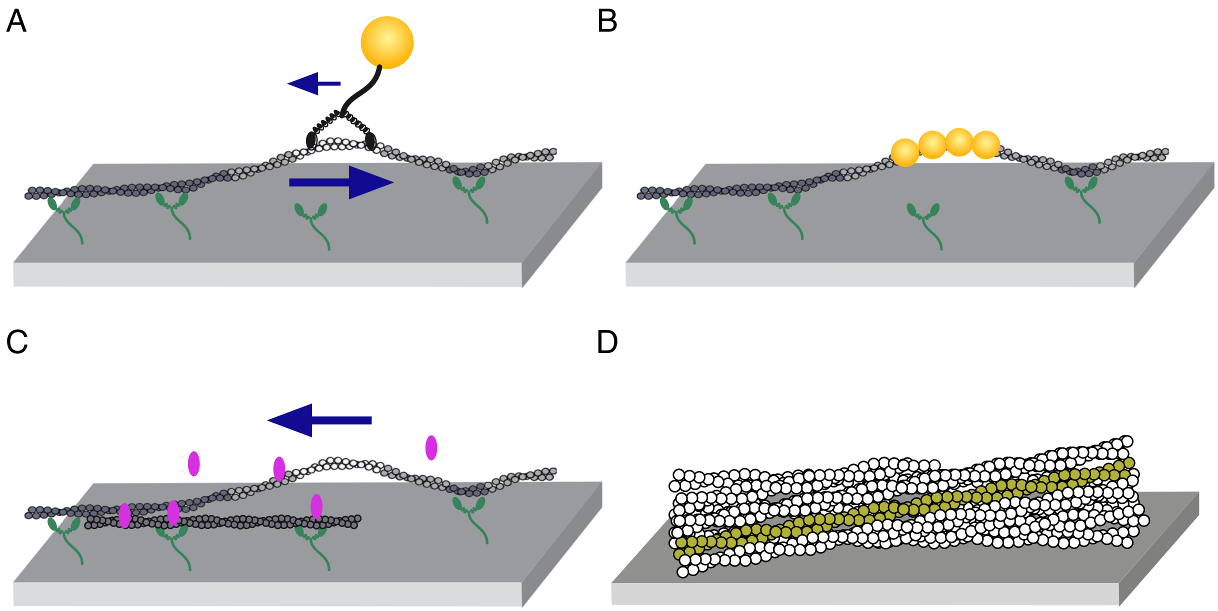

Figure 19. Future directions. (A) Quantum dot labeled myosin-5 walking along the filament propelled by NMIIB. (B) The studies of preference of cofilin for segments of actin under compression. (C) In-line formation of fascin bundles (pink ovals – fascin, green – myosin-6). (D) The supertwist detection in fascin bundles

4.4.2 THE PREFERENCE OF ACTIN-BINDING PROTEINS FOR ACTIN UNDER TENSION OR COMPRESSION

Cofilin is an actin binding protein that binds cooperatively to actin, creates the mechanical discontinuity between bare and cofilin-decorated filaments, and induces actin breaking at the boundary (Elam et al., 2013a). The maximum severing activity is achieved at half saturating concentration of cofilin (Elam et al., 2013b). It has been shown that cofilin severs actin with a delay when the filament is under tension (Hayakawa et al., 2011). Does cofilin target the segments of actin under compression? Both mechanisms, buckling and cofilin binding, can induce severing of actin filaments in vitro (Elam et al., 2013a; Murrell and Gardel, 2012). Is it possible that they could be working synergistically? The set of experiments where TMR-actin or actin labeled with F-tractin (Johnson and Schell, 2009) is pulled by myosins in a FLIC assay, and cofillin is added to the solution can be performed, Figure 19B. If the compressive forces promote cofilin-mediated severing I should see increased actin breaking for the buckled actin segments directly visible in the FLIC assay.

A similar approach can be used to investigate the behavior of the Arp 2/3 complex. Arp 2/3 is an actin binding protein complex that binds to the side of a “mother” filament and nucleates a new branch “daughter filament” (Blanchoin et al., 2014). It was shown to preferentially bind to the convex face of the immobilized, curved filaments (Risca et al., 2012). The authors propose a fluctuation gating model where Arp 2/3 waits for a favorable structural fluctuation in F-actin to occur. Would Arp 2/3 also preferentially bind actin under compression? The FLIC assay could be set up in a standard way (myosins immobilized to the surface, actin gliding on top of them), however, in the presence of a low concentration of fluorescently labeled Arp2/3. Alternatively, the experiment can be performed with non-labeled Arp2/3 but in a presence of low concentration of labeled G-actin (monomeric actin). The branch formation or Arp2/3 binding to actin could be directly observed in the assay. The frequency of branch formation from the buckled segments of actin versus non-buckled segments would provide an insight into the preference of Arp 2/3 for the actin under different mechanical states.

4.4.3 THE FLEXIBILITY AND STRUCTURE OF FASCIN-ACTIN BUNDLES

In this thesis actin filaments gliding was studied in a FLIC assay. The myosin binding in gliding filament assay geometry leads to substantial change in actin shape (the segment of actin has to be brought closer to the surface). The buckled and tensed segments of actin are observed. It would be interesting to see how actin bundles of different size behave in the FLIC assay.

Fascin is an actin binding protein that crosslinks actin filaments to form parallel bundles. Fascin-actin bundles do not grow *in vitro* above 20-filaments thickness (Claessens et al., 2008). Claessens and colleagues propose that fascin changes the helical twist of F-actin and impose the geometrical restrain on packaging of individual actin filaments in a bundle. The change of helical twist of F-actin potentially could lead to super-twisting of the filaments in a bundle.

To detect the presence of actin super-twisting in fascin-actin bundles the in-line bundle formation experiment can be performed (Figure 19C). The FLIC assay would be set-up in a standard way, however fascin would be added to the solution. It is expected that fascin-decorated filaments passing close to each other would bundle (if they are oriented in the same direction). The real time observation of this process could reveal super-twisting of the filaments, as demonstrated by my ability to observe the handedness of an actin plectoneme in Chapter 3. Alternatively, the twist in a static bundle could be investigated (Figure 19D). Bundles can be formed from the filaments labeled in two different colors (95% filaments labeled in one color and 5 % labeled in the other). The ratio of 95% versus 5% should result in an average of one labelled filament per bundle. When the two-color bundle is placed at the reflective surface (Figure 19D), the super-twist should be detectable as a pattern of dimmer and bright fluorescence of the labeled filament. This pattern would arise from the filament being wrapped around other filaments and as a consequence being tilted with the respect to the surface.

CHAPTER 5: MATERIALS AND METHODS

5.1 EXPERIMENTAL METHODS

5.1.1 MYOSIN CONSTRUCTS AND PROTEIN REAGENTS

The myosin-6-HMM-GCN4-Flag-Ctag construct and myosin-6-HMM-GCN4-Flag-YFP construct (used only for data presented in Figure 8B) contained porcine myosin 6 (GeneBank accession number XP_005659483, amino acids 1-994). The myosin-5-HMM-GCN4-Flag-Ctag construct and myosin-5-HMM-GCN4-YFP-Flag construct (used for data presented in Figure 12, 13, 14) contained the first 1107 amino acids of chicken myosin-5a. Myosin-5-Ctag and myosin-6-Ctag constructs were expressed using recombinant baculovirus in Sf9 insect cells. Myosin-5-YFP and myosin-6-YFP constructs were expressed in Sf9 insect cells using the Insect Direct expression system. All the myosin-5 and myosin-6 constructs were co-expressed with baculovirus containing calmodulin and the light-chain MLC-1sa from human. The NMIIB-GFP-Flag HMM construct contained chicken NMIIB amino acids 1-1228 (GeneBank accession number M93676, no splice insert). NMIIB was co-expressed with regulatory and essential light chains (BLC) using baculovirus expression system in Sf9 insect cells.

Myosin light chain kinase was purified from human platelets as previously described (Adelstein and Klee, 1981). Affinity clamp protein was expressed and purified from bacterial culture as previously described (Huang et al., 2009, 2008). Calmodulin was expressed and purified from bacterial culture as previously described (Gopalakrishna and

Anderson, 1985). Actin was purified from chicken breasts as previously described in and polymerized to F-actin at 10 μM monomer concentration as described in (Pardee and Spudich, 1982). Here, 1% of biotinylated actin monomers (labeled at Cys 374 by biotin-maleimide (Rock et al., 2000; Zimmermann et al., 2015)) was used.

5.1.2 MYOSIN PURIFICATION SCHEME

All the myosins were purified using Flag affinity chromatography. The complete purification protocol for NMIIB was described by Norstrom et. al (Norstrom et al., 2010), therefore the following procedure describes the purification of myosin-5 and myosin-6. Briefly, Sf9 cells were infected with the appropriate baculovirus and cultured for 48h. Cells were harvested by centrifugation and resuspended in lysis buffer (50 mM Tris pH 7.7, 150 mM KCl, 4 mM $MgCl_2$, 0.5 mM EDTA, 1 mM EGTA, 0.1% Triton X-100, 7% sucrose, 2 mM ATP and protease inhibitors). The cells were freeze-thawed and nutated for 30 minutes at 4°C to allow the myosin to dissociate from actin. The lysate was spun down and the supernatant was incubated with the anti-Flag resin (Sigma) for 1 hour at 4°C with nutation. The resin was pulled down by either light spin or gravitationally and resuspended in wash buffer (20 mM imidazole pH 7.5, 150 mM KCl, 5 mM $MgCl_2$, 1 mM EDTA, 1 mM EGTA, 3 mM ATP, 0.5 mM DTT and protease inhibitors). The Pierce drip column was assembled and the anti-Flag resin was transferred to the column. The resin was extensively washed and then the column was capped and incubated for 1 hour at 4°C with a wash buffer containing 0.2 mg/ml Flag peptide. The elution was collected and dialyzed over night against dialysis buffer (25 mM imidazole pH 7.5, 1 mM EGTA, 4 mM $MgCl_2$, 150 mM KCl, 50% glycerol, 1 mM DTT). The myosins were stored at -20 °C.

5.1.3 SILICON WAFER PREPARATION

Mechanical grade silicon wafers coated with a 1-1.7 nm thick layer of silicon oxide were cleaned extensively with acetone and methanol. The additional layer of silicon oxide was deposited, to the desired final thickness reported in the main text, using AJA Orion 5 UHV sputtering system. The thickness of silicon oxide layer was measured by ellipsometry using a Gaertner Waferskan Ellipsometer. Between assays, the silicon wafers were cleaned by piranha solution.

5.1.3 FLIC ASSAY

The flow cell was constructed from silicon wafer coated with ~20 nm SiO_2 layer (except for data presented in Figure 8B, 9A, 12, 13, 14, 17, 18 where the SiO_2 thickness was ~1.7 nm), two pieces of double-sided tape, and glass coverslip. Flow cells were incubated with affinity clamp protein (0.33 mg/ml in phosphate-buffered saline pH 7.3: 137 mM NaCl, 2.7 mM KCl, 4.3 mM $Na_2HPO_4 \bullet 7H_2O$, 1.4 mM KH_2PO_4 ; 2 min) or with anti-GFP (0.05 mg/ml in PBS), followed by a bovine serum albumin block (1 mg/ml in Assay Buffer, AB, 2 min). The composition of AB buffer was: 25 mM imidazole, pH 7.5, 25 mM KCl, 1 mM EGTA, 4 mM $MgCl_2$, 10 mM dithiothreitol. Myosin 6 was added to the flow cell at the concentrations indicated in the main text (10 µl of the myosin diluted in AB, 2 min). The flow cell was rinsed extensively with AB. Then, 20 nM F-actin stabilized with tetramethylrhodamine-phalloidin (Sigma) or Atto647N-phalloidin (ATTO-TEC, data presented in Figure 8B, 9A, 12, 13, 14) was added and incubated for 2 min. The flow cell was washed and static filaments were imaged in the AB buffer containing 0.086 mg/ml glucose oxidase, 0.014 mg/ml catalase, and 0.09 mg/ml glucose. For moving filaments, the motility buffer (2 mM ATP, 0.086 mg/ml glucose oxidase, 0.014 mg/ml catalase, and 0.09 mg/ml glucose in AB) was added. Imaging was performed using a Zeiss Axiovert 200 microscope with an Andor Luca camera and Olympus 63x 1.2 water immersion objective.

5.2 DATA ANALYSIS

5.2.1 FILAMENT TRACKING

Filaments were traced using a semi-automated, custom ImageJ script. The initial steps were described in (Graham et al., 2014). Briefly, background subtraction, smoothing and contrast enhancement was performed in ImageJ using built-in functions. Then, the threshold was set to highlight only the filaments and the images were skeletonized using ImageJ built-in functions, as in (Graham et al., 2014). The ROI selection for a single filament was created for each frame of the movie using the wand tool. Notice that from now on a single filament was processed at a time. The pixels selected by the wand tool were ordered from the ends to create a “path” covering the entire length of the filament. The nodes were selected along the “path” to transform it into a segmented line ROI. A set of segmented line ROIs was used to create a kymograph (Pollard lab pluggin, kindly provided by David Kovar). Notice that this procedure makes an individual selection for each frame of a movie (as opposed to extending the previous selection). It is suitable to be used at low myosin surface density when the filaments are floppy. Thresholds were adjusted as needed to identify and trace actin filaments in the case of significant fluctuations of fluorescence intensity for a single actin filament. Manual corrections were introduced when needed.

5.2.2 FLIC CALIBRATION

For FLIC calibration shown in Figure 7B, the FLIC assay was set up as described above, loading myosin 6 into the flow chamber at 41.9 nM and using silicon wafers coated with SiO_2 layer of different thickness (1.7, 20.2, 78.2, 115.6, 139.5 nm). For each condition 18-20 static filaments were manually traced in ImageJ. Background selections were also drawn. The average intensity value of the top 20% brightest pixels in the filament tracings, corrected by the average intensity value of the bottom 20% of "background pixels" was reported for each condition: $I(h_{SiO_2})$ = Average $_{\text{filaments TOP 20\%}}$ - Average $_{\text{background BOTTOM 20\%}}$. The intensity values were fitted to the equation 1, as previously reported in (Persson et al., 2010) (E-1):

$$I(h_{SiO_2}) = I_1 + I_2\left(sin^2\left(2\pi\frac{n_{SiO_2}\times h_{SiO_2}+n\times h}{\lambda_{Ex}}\right)\times sin^2\left(2\pi\frac{n_{SiO_2}\times h_{SiO_2}+n\times h}{\lambda_{Em}}\right)\right)$$

where I_1 and I_2 represent the lowest (baseline) value of intensity and the increase above this value at maximum constructive interference, respectively. Refractive indexes of an aqueous buffer and SiO_2 are n = 1.333 and n_{SiO_2} = 1.46, h is a height of a filament above the SiO_2 surface ("myosin length"), h_{SiO_2} is a thickness of SiO_2 layer, λ_{Ex} and λ_{Em} are excitation and emission wavelength (here λ_{Ex} = 540 nm, λ_{Em} = 570 nm). For the data presented in Fig. 1*B*, the fit was reached with the fit parameters: I_1 = 500, I_2 = 1348.21 and h = 10.44, suggesting that on average un-buckled, static filaments are held by myosin 10.44 nm above the surface. For the filaments presented in 3 C-F, the kymographs were assembled as described in section 5.2.1. The filament intensity values were background corrected (the average of the bottom 20% of the local background pixels was subtracted from each pixel in a kymograph). The height above the surface was calculated by numerically solving the equation E-1 for h.

5.2.3 MYOSIN POSITION ASSIGNMENT

The myosin position assignment was performed either from the raw movies or from the kymographs, depending on the purpose. In both cases the location was manually assigned, taking under the account the intensity of fluorescence, the duration of the attachment and whether or not the attachment can be observed multiple times.

The number of assigned myosins was lower than expected at increasing myosin immobilization concentration. There are two main reasons why it might be: 1) the filaments with more attachments are easier to trace, therefore the trend might be biased towards higher number of motors at low myosin density; 2) at high myosin density the chances of under-counting the motors are higher (Poisson error).

5.2.4 ATTACHMENT TIME DATA ANALYSIS

The myosin attachment times were manually picked from the kymographs as demonstrated in 5C, and plotted against the distance to the nearest attached neighbor. The distances to the nearest neighbor were extracted using custom script in Julia. The data were fitted to the equation 2 (E-2) by maximum likelihood estimation (NLopt package, Julia).

$$T = T_1 e^{-distance/\delta}$$

The 95% confidence intervals were calculated from 1000 bootstrap samples of the same size as the data set (Bootstrap package, Julia).

5.2.5 BUCKLE PICKING PROCEDURE

The limits of a buckle were picked by 1) thresholding a kymograph, 2) creating the ROI selections over the high intensity segments of actin and 3) drawing a rectangle bounding box over each selection (ImageJ, built-in functions). The vertical and horizontal dimensions of a rectangle are a buckle lifetime and buckle length, respectively.

5.2.7 SIMULATIONS

Stochastic simulations of a two-myosin stepping were performed using custom script in Julia. To generate statistically correct time-evolution trajectories of three populations of actin (left, middle, right –see below) in continuous time, we used Gillespie method (Gillespie package, Julia). In our simulations, two myosins are separated by a constant distance *d* and they are allowed to step forward (Figure 11A), pulling the 10 μm long segment of F-actin from left to right. At the time 0 s the length of actin to the left of the two motors (from now on called “left” population) equals to *10 – d* μm, the length of actin between two motors (“middle”) equals to *d* (230 nm, 460 nm, 690 nm, as specified for each simulations) and the length of actin to the right of the two motors (“right”) equals to 0 nm. As the simulation time progresses, myosins take 30 nm steps (Altman et al., 2004) that change the length of actin for each population. The simulations continue until the “left” population reaches 0 nm length (or, less likely, the defined simulation time is over). The myosins take step with an average unloaded rate k = 3.3 s^{-1} (model 2) or with force-dependent rate (k_c) calculated from the formula (model 1)(E-3) (Altman et al., 2004), (see Figure 11B):

$$k_c = \frac{1}{\tau_b + \tau_m e^{\frac{F_c \delta}{k_b T}}}$$

where F_c is hindering force (Euler force produced by buckled segment of actin, see below), k_bT is thermal energy, δ is a distance over which the load acts, and $\tau_b/(\tau_b + \tau_m)$ and $\tau_m/(\tau_b + \tau_m)$ is the fraction of time the unloaded motor spends undergoing biochemical and mechanical cycle (respectively). The Euler force (F_c) is calculated from the Euler equation (for the free ends condition) (Howard, 2001) (E-4)

$$F_c = \frac{\pi^2 EI}{L^2}$$

where EI is flexural rigidity (L_p= EI /k_BT) and L is a contour length of actin. The persistence length of the phalloidin-stabilized actin is L_p = 18 μm, therefore EI = $7.2\times10^{-26} N \cdot m^2$(H. Isambert et al., 1995; Kovar and Pollard, 2004). The Euler force produced by a buckle of given length is shown in Figure 20.

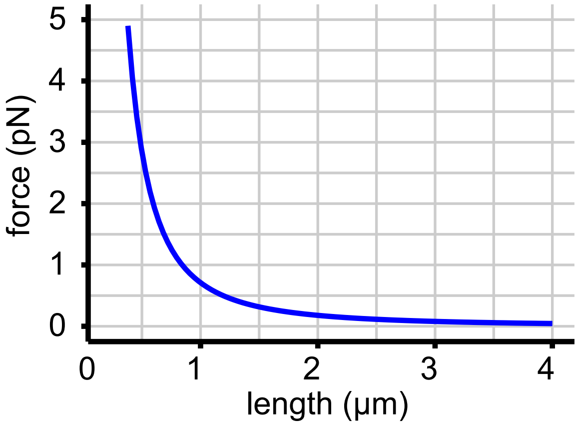

Figure 20. Euler buckling as a function of buckle length. The force was calculated according to equation E-4 for free rotating ends condition.

Note that $k_c(F_c=0) = 3.3\ s^{-1}$. The myosin on the right (the leading motor, experiencing the assisting load) takes steps with an average rate k = 3.3 s^{-1} unless the length of the “middle” segment of actin is shorter then the starting value. In this case the rate of the myosin in the front is set to 0 s^{-1}, consistent with the fact that the hindering force on this motor would be above the stall force ($F_s = -\kappa x$, where κ is a myosin spring constant and x is a displacement from the stationary position). According to Veigel et. al. the cross-bridge stiffness might be as high as κ = 0.69 pN/nm (Veigel et al., 1998).

5.2.8 BUCKLE SHAPE CONSIDERATION

To test whether the buckles produced in the simulations would have enough vertical displacement to be detected in a FLIC assay and therefore can be directly compared to the experimental data, the height above the surface was approximated.

An ellipse can approximate the shape of a buckled actin segment, Figure 21. In our simulations we know the distance between the myosins (d=2*b) and we know the length of actin segment between them (half of the circumference, c/2). It allows us to calculate the peak height of the actin filament above the surface (a).

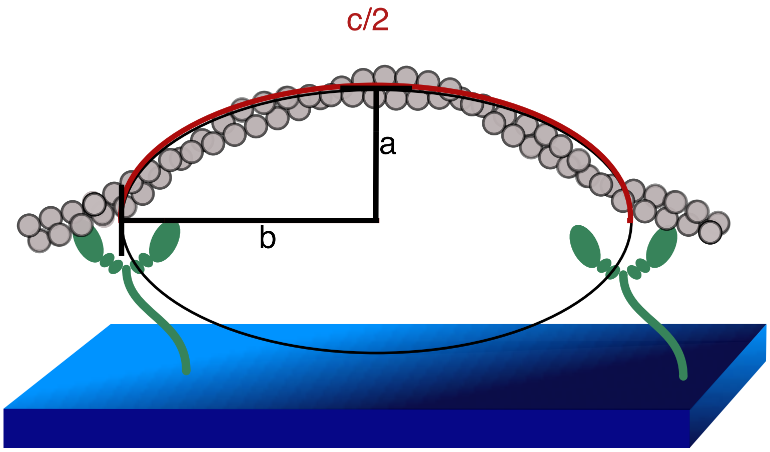

Figure 21. Buckle shape approximation. The distance between two myosins is d = 2*b. The length of actin between the myosins can be approximated as a half of a circumference of an ellipse characterized by the semi-axis a and b.

To check whether a single myosin step could produce a detectable buckle, at different distances between the myosins, we calculated the length of “a”, using an approximation for the circumference proposed by (Ramanujan, 1914) (E-5) :

$$C \approx \pi(a+b)\left(1+\frac{3h}{10+\sqrt{4-3h}}\right)$$

where $h = \frac{(a-b)^2}{(a+b)^2}$ and a and b define the two axis of an ellipse.

For all the distances between the myosins explored in these studies, a single myosin step is enough to lift the actin by 40 nm, Table 2. We picked an arbitrary value of 40 nm as a threshold, because the majority of short buckles obtained at high myosin concentrations oscillate around this value.

Table 1. Buckle height at different values of spacing (distance between the myosins).

distance	c/2 after one step	height above the surface (a)	detectable buckle?
230 nm	260 nm	42 nm	YES
460 nm	490 nm	54 nm	YES
690 nm	720 nm	63 nm	YES

REFERENCES

Adelstein, R.S., Klee, C.B., 1981. Purification and characterization of smooth muscle myosin light chain kinase. J Biol Chem 256, 7501–9.

Ajo-Franklin, C.M., Yoshina-Ishii, C., Boxer, S.G., 2005. Probing the structure of supported membranes and tethered oligonucleotides by fluorescence interference contrast microscopy. Langmuir ACS J. Surf. Colloids 21, 4976–4983. doi:10.1021/la0468388

Ali, M.Y., Kennedy, G.G., Safer, D., Trybus, K.M., Sweeney, H.L., Warshaw, D.M., 2011. Myosin Va and myosin VI coordinate their steps while engaged in an in vitro tug of war during cargo transport. Proc. Natl. Acad. Sci. U. S. A. 108, E535–541. doi:10.1073/pnas.1104298108

Ali, M.Y., Previs, S.B., Trybus, K.M., Sweeney, H.L., Warshaw, D.M., 2013. Myosin VI has a one track mind versus myosin Va when moving on actin bundles or at an intersection. Traffic 14, 70–81. doi:10.1111/tra.12017

Ali, M.Y., Uemura, S., Adachi, K., Itoh, H., Kinosita, K., Ishiwata, S. ’ichi, 2002. Myosin V is a left-handed spiral motor on the right-handed actin helix. Nat Struct Biol 9, 464–7. doi:10.1038/nsb803

Altman, D., Sweeney, H.L., Spudich, J.A., 2004. The mechanism of myosin VI translocation and its load-induced anchoring. Cell 116, 737–49.

Ando, T., Uchihashi, T., Kodera, N., 2013. High-speed AFM and applications to biomolecular systems. Annu. Rev. Biophys. 42, 393–414. doi:10.1146/annurev-biophys-083012-130324

Aschenbrenner, L., Naccache, S.N., Hasson, T., 2004. Uncoated endocytic vesicles require the unconventional myosin, Myo6, for rapid transport through actin barriers. Mol Biol Cell 15, 2253–63. doi:10.1091/mbc.E04-01-0002

Ashkin, A., Dziedzic, J.M., Bjorkholm, J.E., Chu, S., 1986. Observation of a single-beam gradient force optical trap for dielectric particles. Opt. Lett. 11, 288.

Berger, F., Keller, C., Klumpp, S., Lipowsky, R., 2012. Distinct transport regimes for two elastically coupled molecular motors. Phys. Rev. Lett. 108, 208101. doi:10.1103/PhysRevLett.108.208101

Blanchoin, L., Boujemaa-Paterski, R., Sykes, C., Plastino, J., 2014. Actin dynamics, architecture, and mechanics in cell motility. Physiol Rev 94, 235–63. doi:10.1152/physrev.00018.2013

Block, S.M., Blair, D.F., Berg, H.C., 1989. Compliance of bacterial flagella measured with optical tweezers. Nature 338, 514–8.

Block, S.M., Goldstein, L.S., Schnapp, B.J., 1990. Bead movement by single kinesin molecules studied with optical tweezers. Nature 348, 348–52. doi:10.1038/348348a0

Braun, D., Fromherz, P., 1998. Fluorescence Interferometry of Neuronal Cell Adhesion on Microstructured Silicon. Phys Rev Lett 81, 5241–5244. doi:10.1103/PhysRevLett.81.5241

Buss, F., Arden, S.D., Lindsay, M., Luzio, J.P., Kendrick-Jones, J., 2001. Myosin VI isoform localized to clathrin-coated vesicles with a role in clathrin-mediated endocytosis. EMBO J 20, 3676–84. doi:10.1093/emboj/20.14.3676

Cai, Y., Biais, N., Giannone, G., Tanase, M., Jiang, G., Hofman, J.M., Wiggins, C.H., Silberzan, P., Buguin, A., Ladoux, B., Sheetz, M.P., 2006. Nonmuscle myosin IIA-dependent force inhibits cell spreading and drives F-actin flow. Biophys. J. 91, 3907–3920. doi:10.1529/biophysj.106.084806

Capitanio, M., Canepari, M., Maffei, M., Beneventi, D., Monico, C., Vanzi, F., Bottinelli, R., Pavone, F.S., 2012. Ultrafast force-clamp spectroscopy of single molecules reveals load dependence of myosin working stroke. Nat Methods 9, 1013–9. doi:10.1038/nmeth.2152

Cheney, R.E., O'Shea, M.K., Heuser, J.E., Coelho, M.V., Wolenski, J.S., Espreafico, E.M., Forscher, P., Larson, R.E., Mooseker, M.S., 1993. Brain myosin-V is a two-headed unconventional myosin with motor activity. Cell 75, 13–23.

Claessens, M.M.A.E., Semmrich, C., Ramos, L., Bausch, A.R., 2008. Helical twist controls the thickness of F-actin bundles. Proc Natl Acad Sci U A 105, 8819–22. doi:10.1073/pnas.0711149105

Clemen, A.E.-M., Vilfan, M., Jaud, J., Zhang, J., Bärmann, M., Rief, M., 2005. Force-dependent stepping kinetics of myosin-V. Biophys J 88, 4402–10. doi:10.1529/biophysj.104.053504

de la Cruz, E.M., Ostap, E.M., 2004. Relating biochemistry and function in the myosin superfamily. Curr Opin Cell Biol 16, 61–7. doi:10.1016/j.ceb.2003.11.011

Efremov, A.K., Radhakrishnan, A., Tsao, D.S., Bookwalter, C.S., Trybus, K.M., Diehl, M.R., 2014. Delineating cooperative responses of processive motors in living cells. Proc. Natl. Acad. Sci. U. S. A. 111, E334–343. doi:10.1073/pnas.1313569111

Elam, W.A., Kang, H., De la Cruz, E.M., 2013a. Biophysics of actin filament severing by cofilin. FEBS Lett 587, 1215–9. doi:10.1016/j.febslet.2013.01.062

Elam, W.A., Kang, H., De La Cruz, E.M., 2013b. Competitive displacement of cofilin can promote actin filament severing. Biochem Biophys Res Commun 438, 728–31. doi:10.1016/j.bbrc.2013.07.109

Frank, D.J., Noguchi, T., Miller, K.G., 2004. Myosin VI: a structural role in actin organization important for protein and organelle localization and trafficking. Curr Opin Cell Biol 16, 189–94. doi:10.1016/j.ceb.2004.02.001

Gebhardt, J.C.M., Clemen, A.E.-M., Jaud, J., Rief, M., 2006. Myosin-V is a mechanical ratchet. Proc Natl Acad Sci USA 103, 8680–5. doi:10.1073/pnas.0510191103

Gillespie, D.T., 1977. Exact stochastic simulation of coupled chemical reactions. J. Phys. Chem. 81, 2340–2361. doi:10.1021/j100540a008

Gopalakrishna, R., Anderson, W.B., 1985. Monovalent cation-insensitive hydrophobic region on calmodulin facilitates the rapid isolation and quantitation of calmodulin free from other Ca2+-dependent hydrophobic proteins. J. Appl. Biochem. 7, 311–322.

Graham, J.S., McCullough, B.R., Kang, H., Elam, W.A., Cao, W., De La Cruz, E.M., 2014. Multi-platform compatible software for analysis of polymer bending mechanics. PLoS One 9, e94766. doi:10.1371/journal.pone.0094766

Gross, S.P., Vershinin, M., Shubeita, G.T., 2007. Cargo transport: two motors are sometimes better than one. Curr Biol 17, R478–86. doi:10.1016/j.cub.2007.04.025

Hammer, J.A., Sellers, J.R., 2012. Walking to work: roles for class V myosins as cargo transporters. Nat. Rev. Mol. Cell Biol. 13, 13–26. doi:10.1038/nrm3248

Hariadi, R.F., Cale, M., Sivaramakrishnan, S., 2014. Myosin lever arm directs collective motion on cellular actin network. Proc Natl Acad Sci U A. doi:10.1073/pnas.1315923111

Hayakawa, K., Tatsumi, H., Sokabe, M., 2011. Actin filaments function as a tension sensor by tension-dependent binding of cofilin to the filament. J. Cell Biol. 195, 721–727. doi:10.1083/jcb.201102039

Howard, J., 2001. Mechanics of motor proteins and the cytoskeleton. Sinauer Associates, Inc., Sunderland, MA.

Huang, J., Koide, A., Makabe, K., Koide, S., 2008. Design of protein function leaps by directed domain interface evolution. Proc Natl Acad Sci U A 105, 6578–83. doi:10.1073/pnas.0801097105

Huang, J., Nagy, S.S., Koide, A., Rock, R.S., Koide, S., 2009. A Peptide tag system for facile purification and single-molecule immobilization. Biochemistry (Mosc.) 48, 11834–6. doi:10.1021/bi901756n

Hundt, N., Steffen, W., Pathan-Chhatbar, S., Taft, M.H., Manstein, D.J., 2016. Load-dependent modulation of non-muscle myosin-2A function by tropomyosin 4.2. Sci Rep 6, 20554. doi:10.1038/srep20554

Isambert, H., Venier, P., Maggs, A.C., Fattoum, A., Kassab, R., Pantaloni, D., Carlier, M.F., 1995. Flexibility of actin filaments derived from thermal fluctuations. Effect of bound nucleotide, phalloidin, and muscle regulatory proteins. J Biol Chem 270, 11437–44.

Isambert, H., Venier, P., Maggs, A.C., Fattoum, A., Kassab, R., Pantaloni, D., Carlier, M.F., 1995. Flexibility of actin filaments derived from thermal fluctuations. Effect of bound nucleotide, phalloidin, and muscle regulatory proteins. J. Biol. Chem. 270, 11437–11444.

Jewell, B.R., Wilkie, D.R., 1958. An analysis of the mechanical components in frog’s striated muscle. J. Physiol. 143, 515–540.

Johnson, H.W., Schell, M.J., 2009. Neuronal IP3 3-kinase is an F-actin-bundling protein: role in dendritic targeting and regulation of spine morphology. Mol. Biol. Cell 20, 5166–5180. doi:10.1091/mbc.E09-01-0083

Kellerman, K.A., Miller, K.G., 1992. An unconventional myosin heavy chain gene from Drosophila melanogaster. J Cell Biol 119, 823–34.

Kerssemakers, J., Howard, J., Hess, H., Diez, S., 2006. The distance that kinesin-1 holds its cargo from the microtubule surface measured by fluorescence interference contrast microscopy. Proc Natl Acad Sci USA 103, 15812–7. doi:10.1073/pnas.0510400103

Kiessling, V., Tamm, L.K., 2003. Measuring distances in supported bilayers by fluorescence interference-contrast microscopy: polymer supports and SNARE proteins. Biophys. J. 84, 408–418. doi:10.1016/S0006-3495(03)74861-9

Kodera, N., Yamamoto, D., Ishikawa, R., Ando, T., 2010. Video imaging of walking myosin V by high-speed atomic force microscopy. Nature 468, 72–6. doi:10.1038/nature09450

Kohler, F., Rohrbach, A., 2015. Synchronization of elastically coupled processive molecular motors and regulation of cargo transport. Phys. Rev. E Stat. Nonlin. Soft Matter Phys. 91, 012701. doi:10.1103/PhysRevE.91.012701

Kovar, D.R., Pollard, T.D., 2004. Insertional assembly of actin filament barbed ends in association with formins produces piconewton forces. Proc Natl Acad Sci USA 101, 14725–30. doi:10.1073/pnas.0405902101

Kron, S.J., Spudich, J.A., 1986. Fluorescent actin filaments move on myosin fixed to a glass surface. Proc Natl Acad Sci USA 83, 6272–6.

Lambacher, A., Fromherz, P., 1996. Fluorescence interference-contrast microscopy on oxidized silicon using a monomolecular dye layer. Appl. Phys. A 63, 207–216. doi:10.1007/BF01567871

Lo, C.-M., Buxton, D.B., Chua, G.C.H., Dembo, M., Adelstein, R.S., Wang, Y.-L., 2004. Nonmuscle myosin IIb is involved in the guidance of fibroblast migration. Mol Biol Cell 15, 982–9. doi:10.1091/mbc.E03-06-0359

Lu, H., Efremov, A.K., Bookwalter, C.S., Krementsova, E.B., Driver, J.W., Trybus, K.M., Diehl, M.R., 2012. Collective dynamics of elastically coupled myosin V motors. J. Biol. Chem. 287, 27753–27761. doi:10.1074/jbc.M112.371393

Luo, T., Mohan, K., Iglesias, P.A., Robinson, D.N., 2013. Molecular mechanisms of cellular mechanosensing. Nat Mater 12, 1064–71. doi:10.1038/nmat3772

Lymn, R.W., Taylor, E.W., 1971. Mechanism of adenosine triphosphate hydrolysis by actomyosin. Biochemistry (Mosc.) 10, 4617–24.

Mehta, A.D., Rock, R.S., Rief, M., Spudich, J.A., Mooseker, M.S., Cheney, R.E., 1999. Myosin-V is a processive actin-based motor. Nature 400, 590–3. doi:10.1038/23072

Mehta, A.D., Rock, R.S., Rief, M., Spudich, J.A., Mooseker, M.S., Cheney, R.E., 1999. Myosin-V is a processive actin-based motor. Nature 400, 590–593. doi:10.1038/23072

Mermall, V., Miller, K.G., 1995. The 95F unconventional myosin is required for proper organization of the Drosophila syncytial blastoderm. J. Cell Biol. 129, 1575–1588.

Morano, I., Chai, G.X., Baltas, L.G., Lamounier-Zepter, V., Lutsch, G., Kott, M., Haase, H., Bader, M., 2000. Smooth-muscle contraction without smooth-muscle myosin. Nat. Cell Biol. 2, 371–375. doi:10.1038/35014065

Murrell, M., Oakes, P.W., Lenz, M., Gardel, M.L., 2015. Forcing cells into shape: the mechanics of actomyosin contractility. Nat. Rev. Mol. Cell Biol. 16, 486–498. doi:10.1038/nrm4012

Murrell, M.P., Gardel, M.L., 2012. F-actin buckling coordinates contractility and severing in a biomimetic actomyosin cortex. Proc Natl Acad Sci U A 109, 20820–5. doi:10.1073/pnas.1214753109

Nagy, S., Ricca, B.L., Norstrom, M.F., Courson, D.S., Brawley, C.M., Smithback, P.A., Rock, R.S., 2008. A myosin motor that selects bundled actin for motility. Proc Natl Acad Sci U A 105, 9616–9620. doi:10.1073/pnas.0802592105

Nelson, S.R., Trybus, K.M., Warshaw, D.M., 2014. Motor coupling through lipid membranes enhances transport velocities for ensembles of myosin Va. Proc. Natl. Acad. Sci. U. S. A. 111, E3986–3995. doi:10.1073/pnas.1406535111

Niederman, R., Pollard, T.D., 1975. Human platelet myosin. II. In vitro assembly and structure of myosin filaments. J Cell Biol 67, 72–92.

Nitzsche, B., Ruhnow, F., Diez, S., 2008. Quantum-dot-assisted characterization of microtubule rotations during cargo transport. Nat Nanotechnol 3, 552–6. doi:10.1038/nnano.2008.216

Noguchi, T., Lenartowska, M., Miller, K.G., 2006. Myosin VI stabilizes an actin network during Drosophila spermatid individualization. Mol Biol Cell 17, 2559–71. doi:10.1091/mbc.E06-01-0031

Norstrom, M.F., Smithback, P.A., Rock, R.S., 2010. Unconventional processive mechanics of non-muscle myosin IIB. J Biol Chem 285, 26326–34. doi:10.1074/jbc.M110.123851

Odronitz, F., Kollmar, M., 2007. Drawing the tree of eukaryotic life based on the analysis of 2,269 manually annotated myosins from 328 species. Genome Biol 8. doi:10.1186/gb-2007-8-9-r196

Okten, Z., Churchman, L.S., Rock, R.S., Spudich, J.A., 2004. Myosin VI walks hand-over-hand along actin. Nat Struct Mol Biol 11, 884–7. doi:10.1038/nsmb815

Pardee, J.D., Spudich, J.A., 1982. Purification of muscle actin. Methods Cell Biol 24, 271–89.

Park, H., Ramamurthy, B., Travaglia, M., Safer, D., Chen, L.-Q., Franzini-Armstrong, C., Selvin, P.R., Sweeney, H.L., 2006. Full-length myosin VI dimerizes and moves processively along actin filaments upon monomer clustering. Mol Cell 21, 331–6. doi:10.1016/j.molcel.2005.12.015

Persson, M., Albet-Torres, N., Ionov, L., Sundberg, M., Höök, F., Diez, S., M\a ansson, A., Balaz, M., 2010. Heavy meromyosin molecules extending more than 50 nm above adsorbing electronegative surfaces. Langmuir 26, 9927–36. doi:10.1021/la100395a

Ramanujan, 1914. Modular Equations and Approximations to π. Quart. J. Pure App. Math 45, 350–372.

Rhee, A.Y., Ogut, O., Brozovich, F.V., 2006. Nonmuscle myosin, force maintenance, and the tonic contractile phenotype in smooth muscle. Pflüg. Arch. Eur. J. Physiol. 452, 766–774. doi:10.1007/s00424-006-0091-4

Risca, V.I., Wang, E.B., Chaudhuri, O., Chia, J.J., Geissler, P.L., Fletcher, D.A., 2012. Actin filament curvature biases branching direction. Proc. Natl. Acad. Sci. U. S. A. 109, 2913–2918. doi:10.1073/pnas.1114292109

Rochlin, M.W., Itoh, K., Adelstein, R.S., Bridgman, P.C., 1995. Localization of myosin II A and B isoforms in cultured neurons. J. Cell Sci. 108 (Pt 12), 3661–3670.

Rock, R.S., Rice, S.E., Wells, A.L., Purcell, T.J., Spudich, J.A., Sweeney, H.L., 2001. Myosin VI is a processive motor with a large step size. Proc Natl Acad Sci USA 98, 13655–9. doi:10.1073/pnas.191512398

Rock, R.S., Rief, M., Mehta, A.D., Spudich, J.A., 2000. In vitro assays of processive myosin motors. Methods 22, 373–81. doi:10.1006/meth.2000.1089

Rogers, A.R., Driver, J.W., Constantinou, P.E., Kenneth Jamison, D., Diehl, M.R., 2009. Negative interference dominates collective transport of kinesin motors in the absence of load. Phys Chem Chem Phys 11, 4882–9. doi:10.1039/b900964g

Ruhnow, F., Zwicker, D., Diez, S., 2011. Tracking single particles and elongated filaments with nanometer precision. Biophys J 100, 2820–8. doi:10.1016/j.bpj.2011.04.023

Sakamoto, T., Amitani, I., Yokota, E., Ando, T., 2000. Direct observation of processive movement by individual myosin V molecules. Biochem. Biophys. Res. Commun. 272, 586–590. doi:10.1006/bbrc.2000.2819

Sakamoto, T., Webb, M.R., Forgacs, E., White, H.D., Sellers, J.R., 2008. Direct observation of the mechanochemical coupling in myosin Va during processive movement. Nature 455, 128–32. doi:10.1038/nature07188

Schwaiger, I., Sattler, C., Hostetter, D.R., Rief, M., 2002. The myosin coiled-coil is a truly elastic protein structure. Nat. Mater. 1, 232–5. doi:10.1038/nmat776

Schwarz, U.S., Gardel, M.L., 2012. United we stand: integrating the actin cytoskeleton and cell-matrix adhesions in cellular mechanotransduction. J. Cell Sci. 125, 3051–3060. doi:10.1242/jcs.093716

Self, T., Sobe, T., Copeland, N.G., Jenkins, N.A., Avraham, K.B., Steel, K.P., 1999. Role of myosin VI in the differentiation of cochlear hair cells. Dev Biol 214, 331–41. doi:10.1006/dbio.1999.9424

Sellers, J.R., 2000. Myosins: a diverse superfamily. Biochim Biophys Acta 1496, 3–22.

Spudich, J.A., Sivaramakrishnan, S., 2010. Myosin VI: an innovative motor that challenged the swinging lever arm hypothesis. Nat. Rev. Mol. Cell Biol. 11, 128–137. doi:10.1038/nrm2833

Straight, A.F., Cheung, A., Limouze, J., Chen, I., Westwood, N.J., Sellers, J.R., Mitchison, T.J., 2003. Dissecting temporal and spatial control of cytokinesis with a myosin II Inhibitor. Science 299, 1743–1747. doi:10.1126/science.1081412

Sweeney, H.L., Houdusse, A., 2010. Myosin VI rewrites the rules for myosin motors. Cell 141, 573–82. doi:10.1016/j.cell.2010.04.028

Tabb, J.S., Molyneaux, B.J., Cohen, D.L., Kuznetsov, S.A., Langford, G.M., 1998. Transport of ER vesicles on actin filaments in neurons by myosin V. J Cell Sci 111, 3221–34.

Thirumurugan, K., Sakamoto, T., Hammer, J.A., Sellers, J.R., Knight, P.J., 2006. The cargo-binding domain regulates structure and activity of myosin 5. Nature 442, 212–215. doi:10.1038/nature04865

Toepfer, C., Sellers, J.R., 2014. Use of fluorescent techniques to study the in vitro movement of myosins. EXS 105, 193–210. doi:10.1007/978-3-0348-0856-9_9

Tokunaga, M., Kitamura, K., Saito, K., Iwane, A.H., Yanagida, T., 1997. Single molecule imaging of fluorophores and enzymatic reactions achieved by objective-type total internal reflection fluorescence microscopy. Biochem Biophys Res Commun 235, 47–53. doi:10.1006/bbrc.1997.6732

Uyeda, T.Q., Kron, S.J., Spudich, J.A., 1990. Myosin step size. Estimation from slow sliding movement of actin over low densities of heavy meromyosin. J Mol Biol 214, 699–710. doi:10.1016/0022-2836(90)90287-V

Veigel, C., Bartoo, M.L., White, D.C., Sparrow, J.C., Molloy, J.E., 1998. The stiffness of rabbit skeletal actomyosin cross-bridges determined with an optical tweezers transducer. Biophys J 75, 1424–38.

Veigel, C., Schmidt, C.F., 2011. Moving into the cell: single-molecule studies of molecular motors in complex environments. Nat. Rev. Mol. Cell Biol. 12, 163–176. doi:10.1038/nrm3062

Verkhovsky, A.B., Borisy, G.G., 1993. Non-sarcomeric mode of myosin II organization in the fibroblast lamellum. J. Cell Biol. 123, 637–652.

Vicente-Manzanares, M., Koach, M.A., Whitmore, L., Lamers, M.L., Horwitz, A.F., 2008. Segregation and activation of myosin IIB creates a rear in migrating cells. J Cell Biol 183, 543–554. doi:10.1083/jcb.200806030

Vicente-Manzanares, M., Ma, X., Adelstein, R.S., Horwitz, A.R., 2009. Non-muscle myosin II takes centre stage in cell adhesion and migration. Nat Rev Mol Cell Biol 10, 778–90. doi:10.1038/nrm2786

Vicente-Manzanares, M., Zareno, J., Whitmore, L., Choi, C.K., Horwitz, A.F., 2007. Regulation of protrusion, adhesion dynamics, and polarity by myosins IIA and IIB in migrating cells. J Cell Biol 176, 573–580. doi:10.1083/jcb.200612043

Wagner, W., Brenowitz, S.D., Hammer, J.A., 3rd, 2011. Myosin-Va transports the endoplasmic reticulum into the dendritic spines of Purkinje neurons. Nat Cell Biol 13, 40–8. doi:10.1038/ncb2132

Walcott, S., Warshaw, D.M., Debold, E.P., 2012. Mechanical coupling between myosin molecules causes differences between ensemble and single-molecule measurements. Biophys J 103, 501–10. doi:10.1016/j.bpj.2012.06.031

Warner, C.L., Stewart, A., Luzio, J.P., Steel, K.P., Libby, R.T., Kendrick-Jones, J., Buss, F., 2003. Loss of myosin VI reduces secretion and the size of the Golgi in fibroblasts from Snell's waltzer mice. EMBO J. 22, 569–579. doi:10.1093/emboj/cdg055

Wells, A.L., Lin, A.W., Chen, L.Q., Safer, D., Cain, S.M., Hasson, T., Carragher, B.O., Milligan, R.A., Sweeney, H.L., 1999. Myosin VI is an actin-based motor that moves backwards. Nature 401, 505–8. doi:10.1038/46835

Wu, X., Bowers, B., Rao, K., Wei, Q., Hammer JA, null, 1998. Visualization of melanosome dynamics within wild-type and dilute melanocytes suggests a paradigm for myosin V function In vivo. J. Cell Biol. 143, 1899–1918.

Yildiz, A., Forkey, J.N., McKinney, S.A., Ha, T., Goldman, Y.E., Selvin, P.R., 2003. Myosin V walks hand-over-hand: single fluorophore imaging with 1.5-nm localization. Science 300, 2061–5. doi:10.1126/science.1084398

Yildiz, A., Park, H., Safer, D., Yang, Z., Chen, L.-Q., Selvin, P.R., Sweeney, H.L., 2004. Myosin VI steps via a hand-over-hand mechanism with its lever arm undergoing fluctuations when attached to actin. J Biol Chem 279, 37223–6. doi:10.1074/jbc.C400252200

Yu, C., Feng, W., Wei, Z., Miyanoiri, Y., Wen, W., Zhao, Y., Zhang, M., 2009. Myosin VI undergoes cargo-mediated dimerization. Cell 138, 537–48. doi:10.1016/j.cell.2009.05.030

Zimmermann, D., Santos, A., Kovar, D.R., Rock, R.S., 2015. Actin Age Orchestrates Myosin-5 and Myosin-6 Run Lengths. Curr Biol 25, 2057–62. doi:10.1016/j.cub.2015.06.033